**Title**
Novel High Power Density Turn-Less Motor Concept



**Author**
Liu, Christopher Kirby

**Publication Date**
2018

Peer reviewed|Thesis/dissertation

UNIVERSITY OF CALIFORNIA SAN DIEGO

# Novel High Power Density Turn-Less Motor Concept

A Thesis submitted in partial satisfaction of the requirements for the degree Master of Science

in

Electrical Engineering (Medical Devices and Systems)

by

Christopher Kirby Liu

Committee in charge:

Professor Paul K. Yu, Chair
Professor Michael Yip
Professor Vitaliy Lomakin

2018

The Thesis of Christopher Kirby Liu is approved, and it is acceptable in quality and form for publication on microfilm and electronically:

_____

_____

_____

Chair

University of California San Diego

2018

# DEDICATION

This thesis is dedicated to my family and friends whose unwavering love and support made all this possible.

I would additionally like to thank my advisor, Oved Zucker, for guiding and teaching me not only the fundamentals of physics and engineering, but the life lessons and the rich history of the field as well.

TABLE OF CONTENTS

LIST OF FIGURES

LIST OF TABLES

ACKNOWLEDGEMENTS

I would like to acknowledge my on-site thesis advisor, Oved Zucker, for letting me complete my thesis project on his patent and work done on SBIRs previously [1]–[4]. The previous analysis and work on a linear actuator variant at the company, Polarix Corp, served as an invaluable starting point for this project.

I would also like to acknowledge my colleague Thanh Le, who aided in the initial analysis and design of the motor. His insights and support throughout this endeavor are immensely appreciated.

## VITA

2017 Bachelor of Science, University of California San Diego

2018 Master of Science, University of California San Diego

## PUBLICATIONS

Zucker, Oved, Blumenau, Leif, Yu, Paul, Liu, Christopher. "New High Specific Power Motor Technology for All-Electric Class III UAVs" 2018 IEEE Power Modulator and High Voltage Conference, in press.

Zucker, Oved, Yu, Paul, Liu, Christopher. "Advanced Inverter Arrays for Controlled Turn-less Motor (CTM), Semiconductor Limits and MEMS Manufacturing" 2018 IEEE Power Modulator and High Voltage Conference, in press.

Liu, Christopher; Yu, Paul, Zucker Oved, "Experimental Demonstrations of a Representative Motor and Linear Actuator Using Controlled Turn-Less Structure Arrays Motors (CTM)" 2018 IEEE Power Modulator and High Voltage Conference, in press.

ABSTRACT OF THE THESIS

Novel High Power Density Turn-Less Motor Concept

by

Christopher Kirby Liu

Master of Science in Electrical Engineering (Medical Devices and Systems)

University of California San Diego, 2018

Professor Paul K. Yu, Chair

Recent developments in power transistor technologies, particularly with low voltage and high current densities have enabled a redesign of conventional motor technologies. In typical electromechanical devices, multiple turns are used to increase the generated magnetic field of the coil. For motor applications, this results in higher operating voltages in exchange for lower current requirements, as well as larger leakage inductance due to the added volume outside the motor's stator for the return paths of copper. Additionally, the manufacturing of these motors either require complex machinery or costly labor-intensive methods to wind the motors. Alternatively, the Polarix motor-inverter unit relies on cutting-edge semiconductor technologies

to engineer a novel turn-less motor topology. The motor takes advantage of a fortuitous match between current and voltage requirements in a single winding of a motor, to the current and voltage capabilities of high performance transistors. A single motor unit is comprised of 3 conductors (formed in the stator) shorted in a Y configuration and driven by a three-phase inverter. In this topology, we show that a higher power density can be achieved with low total inductance and simplified manufacturing. This thesis serves to demonstrate the viability of this technology on a circular motor – additionally the design, construction and performance is discussed in depth.

# Introduction and Layout

Electric motors were first demonstrated in the early 19th century and have been continuously developed and improved on since then. Currently, electric motors for industrial applications account for around 45% of the total consumed electricity worldwide and that number is significantly higher in more industrialized countries [5]. Additionally, with the recent developments and proliferation of electric cars, drones, and robotics, electric motors will certainly see an even larger rise in their prominence. For these electric drivetrain applications, one of the key performance metrics is the motor's power to weight ratio; thus, the major push in the motor industry, as well as the motivation of this thesis, is to maximize that metric.

Most electric motors convert electrical energy into mechanical energy through the interaction of dynamic magnetic fields with electric currents. This combination between magnetic fields and electric currents to produce a force can be achieved in a wide variety of configurations, as detailed in any motor textbook – whether it be AC or DC, permanent magnet, axial or radial flux, linear, rotary, and so on. A common feature across most modern motors consist of multiple windings, higher applied voltages, and large phase inductances. Current high-performance electric motor technologies are in the range of 5 kW/kg to 10 kW/kg as seen in [6] and [7]. Conversely, our analysis will show an alternative approach to the motor design to achieve up to an order of magnitude larger power to weight ratio. The corresponding metrics of losses, efficiency and cooling requirements will also be addressed.

Chapter 1 will focus on the theory and derivation of a motor's power density and their match to inverter capabilities. Additionally, the motor and inverter design will be reviewed.

Chapter 2 will explore the basic motor analysis and circuit simulations of the motor designed using the previous chapter's analysis.

Chapter 3 will discuss the experimental setup of the circular motor application and the preliminary results.

# Chapter 1: Motor Theory and Derivation

### 1.1 Simple Motor Power Density Derivation

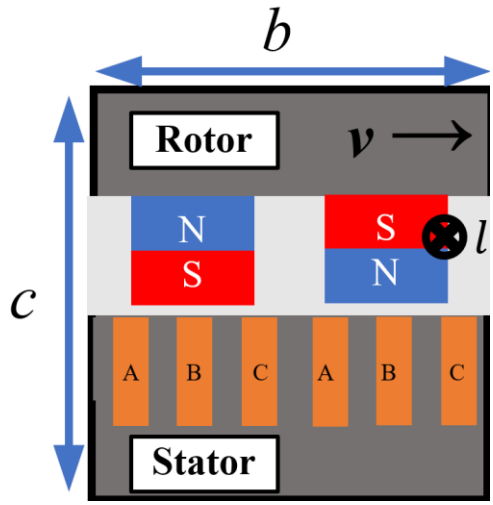


Figure 1: Basic Motor Diagram with pole pair width, b, height, c, and motor length, l, into the page. Stator and rotor are labeled with velocity, v to indicate direction.

The fundamentals of any magnetic based motor stems from Maxwell's equations and the Lorentz force law. The Lorentz force law defines the magnetic force applied to a moving charge (in this case, current in a wire) in a magnetic field:

$$F = I\vec{\boldsymbol{l}} \times \vec{\boldsymbol{B}} \tag{1}$$

Where $F$ is the force produced on a current carrying wire, $I\vec{\boldsymbol{l}}$, when placed in a magnetic field, $\vec{\boldsymbol{B}}$. This describes how a mechanical force can be generated by an electric current to achieve motor work, however, one more equation is needed to complete this description. Faraday's law describes how a time variant magnetic field can produce an electric field, as shown in the following equation – adapted for the motor application using Lenz' law:

$$\nabla \times E = -\frac{\partial \boldsymbol{B}}{\partial t} \quad \rightarrow V = -\frac{d\lambda}{dt} = \frac{d(\boldsymbol{B}A)}{dt} = 2\boldsymbol{B}lv \tag{2}$$

Where $V$ is the induced voltage from the change in magnetic flux, $\boldsymbol{B}A$, which can then be equated to a magnetic field, length, and velocity; the factor of two comes from the fact that two

conductors are being energized at the same time. With these fundamental equations, we can derive a first order approximation of the power output of a motor given its electrical and physical properties, and consequentially, the power density of the motor. This analysis is done assuming a standard three phase motor with permanent magnets in the rotor, however it can be applied to other configurations with some modifications.

Taking equation (1), multiplying by velocity, and considering the geometrical arrangement of the motor with *N* turns, shown in Figure 1, we obtain the following power and power density equation where $\bar{P}$ is the power density of the motor for all three phases:

$$P = F * v = NB\, l\, (2I_{\phi-pk})\, v$$

$$\bar{P} = \frac{P}{Volume} = \frac{2NBI_{\phi-pk}lv}{blc} = \frac{2BI_{\phi-pk}v}{bc} \tag{3}$$

The bar above the power variable indicates that the value is a measure power density and will be used throughout this thesis. Additionally, we can normalize the motor cross sectional dimensions with respect to $b$

$$\bar{P} = \frac{2NBI_{\phi-pk}v}{b^2\bar{c}_b}, \bar{c}_b = \frac{c}{b} \tag{4}$$

From this basic analysis, it is evident that increasing the magnetic field in the rotor, the current in the stator, the number of turns, or the surface velocity, will all yield larger power densities. This relation holds true for most motors regardless of their configuration. Some motors take advantage of mechanical configurations to maximize magnetic field interaction, push for larger surface velocities, or integrate cooling to achieve higher currents, but moving to smaller pole pair widths is not very common. Additionally, all motors incorporate many turns to trade off higher voltages for lower currents in order to yield higher power. However, moving towards small pole pair sizes can be difficult for two main reasons. First, winding many turns in a small pole pair size requires the conductors to be proportionally smaller to fit within the slots – thus increasing

the motor resistance and required cooling. Second, the conductors must be wound into all the slots – requiring a return path outside the active stator area, shown in Figure 2. The portion of the conductors that hang outside of the stator do not contribute flux that couples into the rotor to generate power; this increases the motor volume and weight without any direct contribution to the power. The result of these multiple turn stators yields larger leakage inductance, higher phase resistance, and larger motors (as much as 50% increase in volume). This analysis will instead

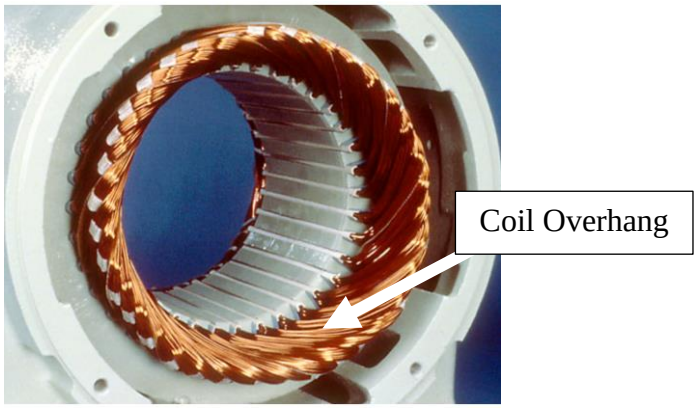


Figure 2: Typical stator with many windings in a three phase motor.[4]

take advantage of the motor pole pair width, $b$, and show that corresponding power density could be much higher than currently available electric motors.

### 1.2 The Turn-less Motor Concept

For a typical three phase two pole motor pictured in Figure 1 and Figure 3a, there are six stator teeth for every two poles; each phase is wound around a tooth and is mirrored across the motor for its return path. A three phase voltage source is connected to the three phases which creates a traveling magnetic field rotating around the motor periphery which acts on the permanent magnets in the rotor. The turn-less motor concept uses these same principles, but removes both the windings on each tooth as well as the winding across the motor for its return

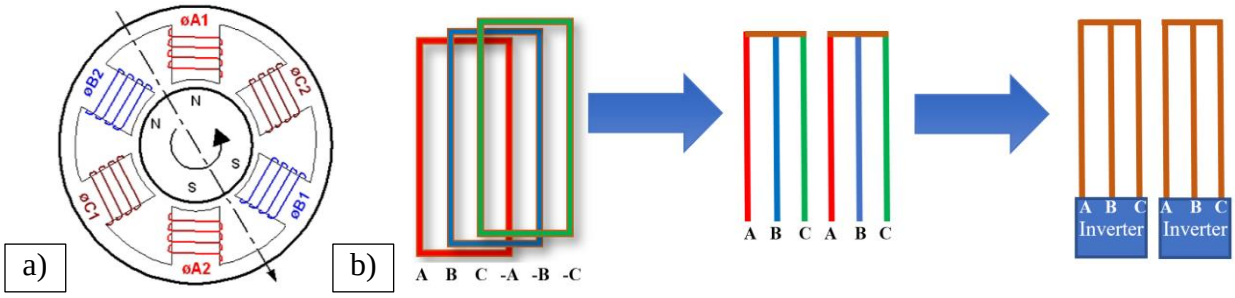


Figure 3: a) Phase winding diagram of a six slot stator and 2 pole rotor. b) Evolution of the typical three phase windings with return paths into the turn-less motor concept with inverters.

path by placing a single conductor in each slot of the motor and shorting every three conductors in a wye configuration as illustrated by Figure 3b.

In this arrangement, a full turn-less motor structure (termed TLS) unit is now formed for every three stator teeth, rather than six teeth. Thus, all the coil overhang, increased resistance, and larger leakage inductance issues mentioned previously for typical motors have been removed at the cost of the winding factor. Each motor unit, with pole pair width, $b$, can be made with much smaller dimensions, yielding larger power densities if everything else remains equal as shown in Eq. (4). The surface area of the conductor relative to the volume increases at smaller pole pair widths, making the motor easier to cool. Now the issue becomes how to input current into the conductors with the return paths removed: 1) wire each unit in parallel and drive them with a single, larger inverter bank, or 2) place a three phase inverter at the end of every three conductors as shown in Figure 3b. The latter option, which is the chosen approach, offers much more reliability than the first option due to the massively parallel structures that can be arrayed

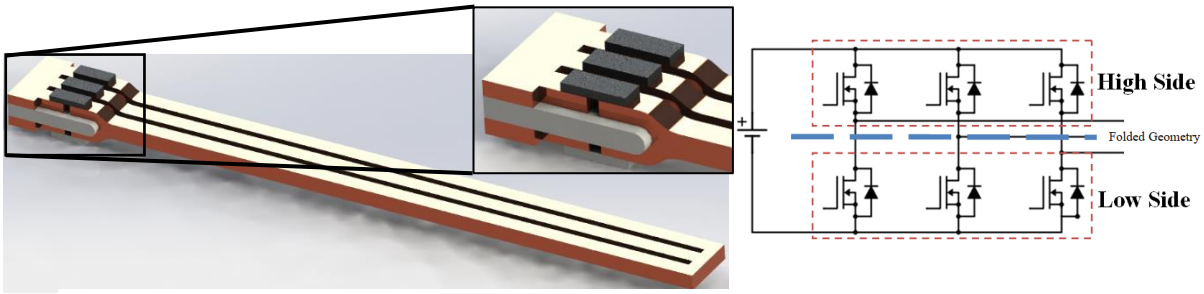


Figure 4: TLS unit connected to a three phase inverter folded over a cooler plate (zoomed box). On the right shows the folded inverter circuit with MOSFET switches.

across a motor. This option has only become viable in recent years due to improved Si and GaN power transistor technologies. Shown in Figure 4 is a diagram of the turn-less motor unit connected to the three phase inverter. The inverter has been designed here to fold over a double sided liquid cooling plate to remove heat from the high side and low side switches. Figure 5 depicts a round motor application built from these TLS units in an array with each unit consisting of three conductors, a three phase inverter, and a pair of permanent magnets.

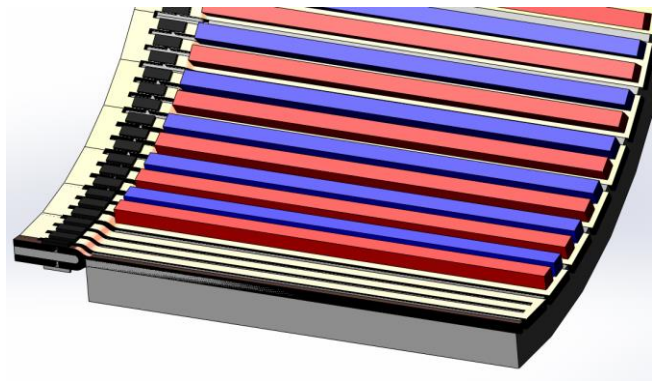

Figure 5: TLS units arrayed along the periphery of a round motor. The red and blue rectangles represent the permanent magnets embedded into the rotor, sitting a small distance above the stator.

### 1.3 Cooling Limited Power Density Analysis

One of the main limiting factors in any motor is the ability to cool the motor. This can be especially difficult in typical motors with large gaps between each winding (also known as the winding fill factor), long coil overhangs, or thicker dielectric to hold voltage across the conductors; each increases the thermal resistance between the copper windings and the cooling source. Typical liquid cooling systems for electric motors pass water through larger areas of the stator via pipes or around the exposed surface of the stator. For simplicity, the following analysis done on the turn-less motor structure will assume that the heat in the stator is generated only by resistive losses and will pass through the outer surface of the stator; yielding a required heat flux ($W/m^2$) that must be removed by some cooling system. There will additionally be a temperature

gradient from the conductor to the surface of the stator which will depend on the insulator used between the conductor and the corresponding surface areas. Eddy current and hysteresis losses will also contribute to the temperature gradient, but these are typically smaller than the resistive losses of the motor with proper design and material selection of the motor laminations. These will be addressed in Chapter 2.

The resistive losses in the conductors of each TLS can described as follows:

$$P_{diss_{TLS}} = I_{\phi-RMS}^2 R \qquad R = \frac{\rho_{Cu} l}{A_{cu}} = \frac{\rho_{Cu} l}{b^2 \bar{A}_{cu}}$$

$$\bar{P}_{diss_{TLS}} = \frac{3P_{diss}}{bl} = \frac{3{I_{\phi-RMS}}^2 \rho_{cu}}{b^3 \bar{A}_{cu}} \tag{5}$$

Where $R$ is the resistance of a single phase, $A_{cu}$ is the cross sectional area of a single conductor, $\bar{A}_{cu}$ is the area normalized to the pole pair width, and $\bar{P}_{diss}$ is the total heat flux in W/m$^2$ passing through the bottom surface area illustrated in Figure 6.

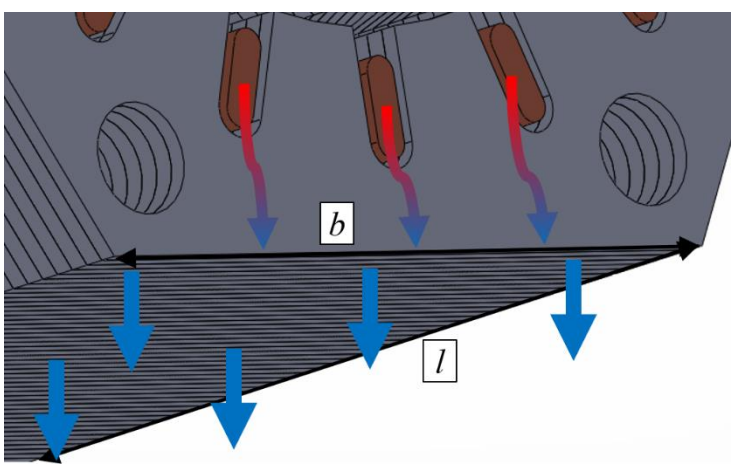


Figure 6: Heat flux as it travels from the conductor to the outer surface of the stator

This equation provides an approximation as to how much heat must be removed from the stator for a given current and pole pair width, which can now be substituted into the power density equation (4) with RMS adjustments for a trapezoidal waveform to obtain:

$$\bar{P}_{TLS} = \frac{Bv}{\bar{c}_b}\left(\frac{2\bar{P}_{diss_{TLS}}}{b}\frac{\bar{A}_{Cu}}{\rho_{Cu}}\right)^{\frac{1}{2}} \tag{6}$$

This equation is very useful as it yields a power density for a given a velocity, magnetic field, heat flux removal, and the pole pair width. These are convenient parameters to work with from an engineering and design point of view because most of them are set by the application or current technologies. The surface velocity of the motor is set by the application of the motor – higher velocities yield higher power densities. The magnetic field in the gap, $B$, is determined by the size of the air gap and strength of the permanent magnet which is typically around 1 – 1.5T depending on the magnet grade [8]. The heat flux needed to be removed, $\bar{P}_{diss}$, from a surface is strongly dependent on the method of cooling chosen and the thermal resistances in the system. Reasonable heat flux numbers using forced air cooling range from .2 – 2 W/cm$^2$ and forced water cooling ranges from 2 – 100+ W/cm$^2$ [9]. Moreover, the pole pair width, $b$, as dictated by this design is constricted by the minimum width of the three phase inverter that would supply current to the motor. This width is limited by the on resistances of the switches and cooling capabilities applied to the inverter. To yield the largest power density in the motor, the inverter must be reduced to very small widths.

### 1.4 Cooling Limited Inverter Capabilities

The width and length required for the three phase inverter is largely dependent on the current, voltage, and power losses that each switch will encounter. To precisely calculate the power losses in this circuit, many circuit parameters must be incorporated into the circuit and solved using SPICE simulations [10]. While this is necessary when designing for a specific

application, this methodology is difficult to employ for this first order analysis. Thus, this approach will run through the power losses in the inverter circuit and simplify the calculation by understanding the current paths during operation.

The control technique for this motor will be a simple six step 120$^{o}$ trapezoidal commutation technique [11]. In this control method, only two phases are energized at a time and produce three phase current waveforms pictured in Figure 7 with the corresponding high side and low side switches shown below. In the ideal case, the torque produced by these currents would be constant, with zero switching time and a perfect trapezoidal flux distribution which is impossible to achieve in practice but is useful for first order calculations.

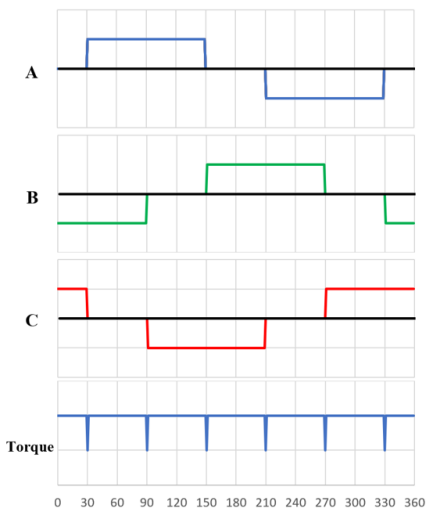


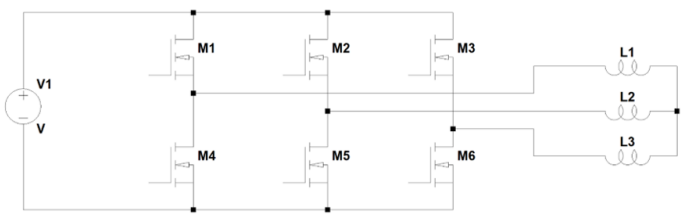


| Step | 1 | 2 | 3 | 4 | 5 | 6 |
|---|---|---|---|---|---|---|
| Angle | 30°-90° | 90°-150° | 150°-210° | 210°-270° | 270°-330° | 330°-30° |
| Switch | M1-M5 | M1-M6 | M2-M6 | M2-M4 | M3-M4 | M3-M5 |

Figure 7: Six-step 120° trapezoidal commutation. Ideal phase currents shown with corresponding motor torque as well as the switching commutation scheme. Note that the current is trapezoidal yielding a "constant" peak current value.

Without getting into the intricacies of MOSFET operation, there are three sources of power loss in MOSFETs: conduction (or ON) losses, body diode losses, and switching losses. Conduction losses are due to the total on resistances in the current path of the MOSFET. Body diode losses occur when the MOSFET conducts in the reverse direction, through the intrinsic body diode rather than the inversion channel. Switching losses occur as the MOSFET is turned

on and off. All three of these losses generate heat in the MOSFET and must be removed to achieve the highest current carrying capabilities of the inverter in the smallest area. To keep this derivation simple, the switching losses will be left out for now, but addressed in Chapter 2.

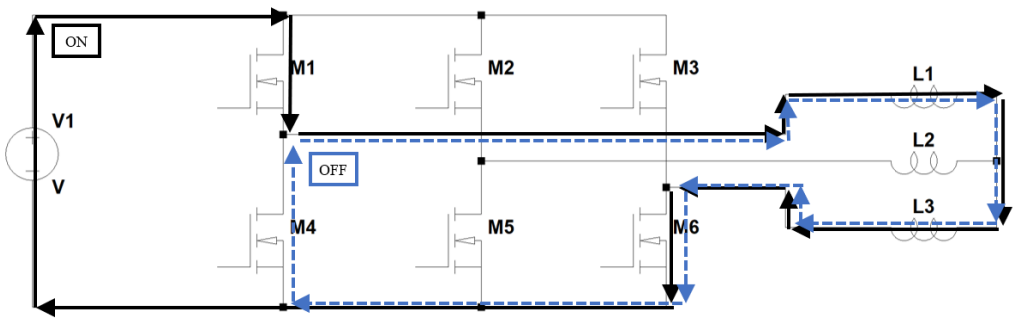


Figure 8: Simplified Turn-less Motor Circuit with trapezoidal commutation. In this case, current flows in the black loop during the on portion of the duty cycle (M1 ON, M6 ON), and in the blue loop during the off portion of the duty cycle (M1 OFF, M6 ON, M4 body diode)

To estimate the power losses in the switches, it is important to understand how current flows through this circuit, as pictured in Figure 8. To produce the rotating magnetic field in the trapezoidal 120$^{o}$ commutation methodology, the inverter cycles through various switching sequences as detailed in [10]. During the ON portion of the duty cycle, current flows in the forward conduction direction of the upper (M1) and lower (M6) MOSFETs. During the off portion of the duty cycle, because the motor acts as an inductive load, the energy stored in the windings' magnetic field, force the current to stay on and conduct through the lower MOSFETs (M4 and M6). Thus, the losses during a single duty cycle for any given switching sequence will have two sources of forward conduction losses from the upper and lower switches (M1 and M6), as well as body diode losses from a single lower switch (M4). With this information, the power losses in the MOSFET and corresponding required cooling can be described as follows:

$$P_{diss_{INV}} = P_{ON} + P_{Diode} + P_{Switching}$$

$$P_{diss_{INV}} = P_{ON} + P_{Diode} = 2 * I_{\phi-pk}{}^2 R_{DS} D + I_{\phi-pk} V_D (1 - D) \quad (7)$$

Where $P_{diss_{INV}}$ is the total power dissipated in the inverter circuit, $I_{\phi-pk}$ is the peak phase current in the motor, $D$ is the average duty cycle the inverter is operating at, and $V_{Diode}$ is the body diode voltage. Lastly, the $R_{DS}$, is the on resistance of the switch, and varies depending on the blocking voltage and technology used for the MOSFET. To estimate the required inverter width, the total losses will be divided by the inverter area to estimate the required cooling.

The $R_{DS}$ of the MOSFET will be assumed using the ideal on resistance of an n-channel silicon unipolar device as detailed in Chapters 1 and 3 of [12]. In this derivation, the on resistance is based on the maximum depletion width of the drift region, mobility, and the doping concentration (see Appendix for derivation). Using the electric field distribution, potential distribution, boundary conditions and some approximations on impact ionization, an analytical solution for the breakdown voltage and depletion width can be found for a given doping concentration. After some algebra, the resultant ideal specific on resistance is determined, as shown in Equation (8):

$$R_{on-sp,ideal} = 5.93 \times 10^{-9}\, BV_{pp}^{2.5} \qquad \Omega \cdot cm^2 \quad (8)$$

Using this equation, the dissipated power in the inverter can now be determined as follows, where $A_{sc}$ is the total area of a single switch which is assumed to be one third of the inverter width, *b*, and some length $l_{inv}$ (Figure 9):

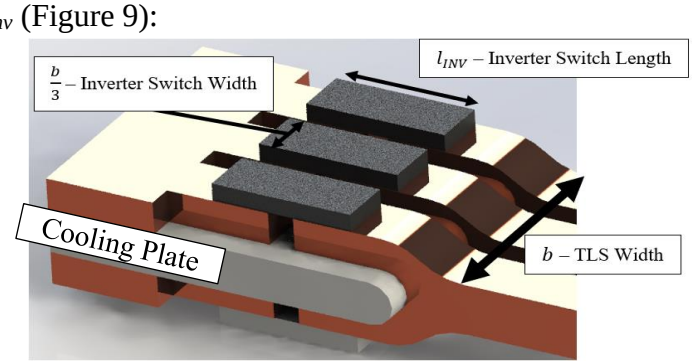


Figure 9: Simplified three-phase inverter diagram with high side and low side switches shown, folded over a cooler plate

$$R_{DS} = \frac{R_{on-sp,ideal}}{A_{sc}} = \frac{R_{on-sp,ideal}}{\frac{b}{3} * l_{inv}} = \frac{3R_{on-sp,ideal}}{bl_{inv}}$$

$$\bar{P}_{diss_{INV}} = \frac{P_{diss_{INV}}}{3bl_{inv}} = 2I_{\phi-pk}^2 D \frac{R_{on-sp,ideal}}{(bl_{inv})^2} + \frac{I_{\phi-pk}\ V_D}{3bl_{inv}}(1-D) \tag{9}$$

Equation (9) details the relation between the power dissipated per area in the inverter for a given width, inverter length, phase current, duty cycle, blocking voltage, and diode voltage. The factor of three in the denominator is introduced because this calculation is an average across a single duty cycle of a single phase, which only conducts a third of the time during actual motor operation. Like the motor analysis, the key limiting factor for the maximum current achieved – and thus power transmitted to the motor – is the ability to remove heat produced by the inverter which is set by the cooling technology. These parameters and equations can be related back to the motor equations (5 and 6) to calculate the maximum achievable power densities of the turn-less motor concept while taking into account limitations of both the motor and inverter capabilities; as detailed in the following section.

## 1.5 Turn-less Motor and Matched Inverter Recap

Table 1 presents the constants and parameters involved in the following analysis. These constants are values that were made in a previous linear actuator experiment.

Table 1: Parameters and Constants

| Parameter | Description | | Units |
|---|---|---|---|
| $v$ | Surface velocity of the rotor | | $\frac{m}{s}$ |
| $l$ | Length of the motor stack | | $m$ |
| $b$ | TLS width or pole pair width | | $m$ |
| $I_{\phi-pk}$ | Peak trapezoidal phase current | | $A$ |
| $I_{\phi-RMS}$ | RMS trapezoidal phase current | | $A$ |
| $P_{TLS}$ | Power output of a single TLS | | $W$ |
| $\bar{P}_{TLS}$ | Power density of a single TLS | | $\frac{W}{m^3}$ |
| $P_{diss_{TLS}}$ | Dissipated power of a single TLS | | $W$ |
| $\bar{P}_{diss_{TLS}}$ | Dissipated power density of a TLS and corresponding cooling power density | | $\frac{W}{m^2}$ |
| $P_{diss_{INV}}$ | Dissipated power of the inverter | | $W$ |
| $\bar{P}_{diss_{INV}}$ | Dissipated power density of the inverter and corresponding cooling power density | | $\frac{W}{m^2}$ |
| $D$ | Duty cycle of the inverter | | % |
| $l_{INV}$ | Length of the inverter switch | | $m$ |
| $R_{on-sp,ideal}$ | Ideal specific on-resistance of a Si MOSFET | | $\Omega \cdot cm^2$ |
| **Constant** | **Description** | **Value** | **Units** |
| $B$ | Effective magnetic field strength of the permanent magnets seen by the conductors | 1 | $T$ |
| $\bar{A}_{cu}$ | Normalized constant of conductor area to TLS width | 0.086 | - |
| $\bar{c}_b$ | Normalized constant of TLS height to TLS width | 1.22 | - |
| $\rho_{Cu}$ | Resistivity of copper | $1.72x10^{-8}$ | Ωm |
| $\rho_{TLS}$ | Average density of TLS | 8000 | $\frac{kg}{m^3}$ |

Table 2 presents the key equations for this analysis for the motor and inverter equations. These derivations all assume a trapezoidal motor and six step trapezoidal current. The explicit derivations not shown previously can be found in the Appendix.

Table 2: Key Equations

| Turn-less Motor and Inverter Equations | | Units |
|---|---|---|
| **Power per TLS Unit** | $P_{TLS} = Bl2I_{\phi-pk} * v$ | $W$ |
| **Power Density** | $\bar{P}_{TLS} = \frac{Bv2I_{\phi-pk}}{\bar{c}_b b^2}$ | $\frac{W}{m^3}$ |
| **Dissipated Power Density – TLS** | $\bar{P}_{diss_{TLS}} = \frac{3{I_{\phi-RMS}}^2\rho_{Cu}}{b^3\bar{A}_{cu}} = \frac{2{I_{\phi-pk}}^2\rho_{Cu}}{b^3\bar{A}_{cu}}$ | $\frac{W}{m^2}$ |
| **Cooling Limited Power Density** | $\bar{P} = \frac{Bv}{\bar{c}_b}\left(\frac{2\bar{A}_{cu}\bar{P}_{diss_{TLS}}}{b\rho_{Cu}}\right)^{\frac{1}{2}}$ | $\frac{W}{m^3}$ |
| **Dissipated Power Density – Inverter** | $\bar{P}_{diss_{INV}} = 2I_{\phi-RMS}^2 D\frac{R_{on-sp,ideal}}{(bl_{inv})^2} + \frac{I_{\phi-RMS}V_D}{3bl_{inv}}(1-D)$ | $\frac{W}{m^2}$ |
| **Specific Power** | $P_{sp} = \frac{\bar{P}_{TLS}}{\rho_{TLS}}$ | $\frac{W}{kg}$ |
| **Motor Efficiency** | $Eff = \frac{1}{1+Y} * 100\%\,; \quad Y = \frac{1}{Bv}\left(\frac{\bar{P}_{diss_{MOT}}\rho_{cu}}{2b\bar{A}_{cu}}\right)^{\frac{1}{2}}$ | % |

The plots given in Figure 10 reflect the geometries and constants (see Table 1) achieved for the linear actuator motor extrapolated to varying surface velocities and TLS widths. Highlighted by the data point in Figure 10a is the specific power of 18.6 kW/kg of the constructed motor with air cooling, a width of 6.6 mm, and surface velocity of 105 m/s. This velocity is close to what the surface velocity could be for electric drivetrains in rotational motors of cars or aerial vehicles. With improved water cooling shown in Figure 10d ($\bar{P}_{diss_{MOT}} = 5\frac{W}{cm^2}$), a specific power of 93 kW/kg can be achieved, which is around an order of magnitude higher than current motor technologies. At these large velocities, the efficiencies of this motor topology, seen in Figure 10be, are still very large due to the resistive losses in the motor being much smaller than the power output. The third plot for both cases, show the peak phase current that the inverter must supply to the TLS.

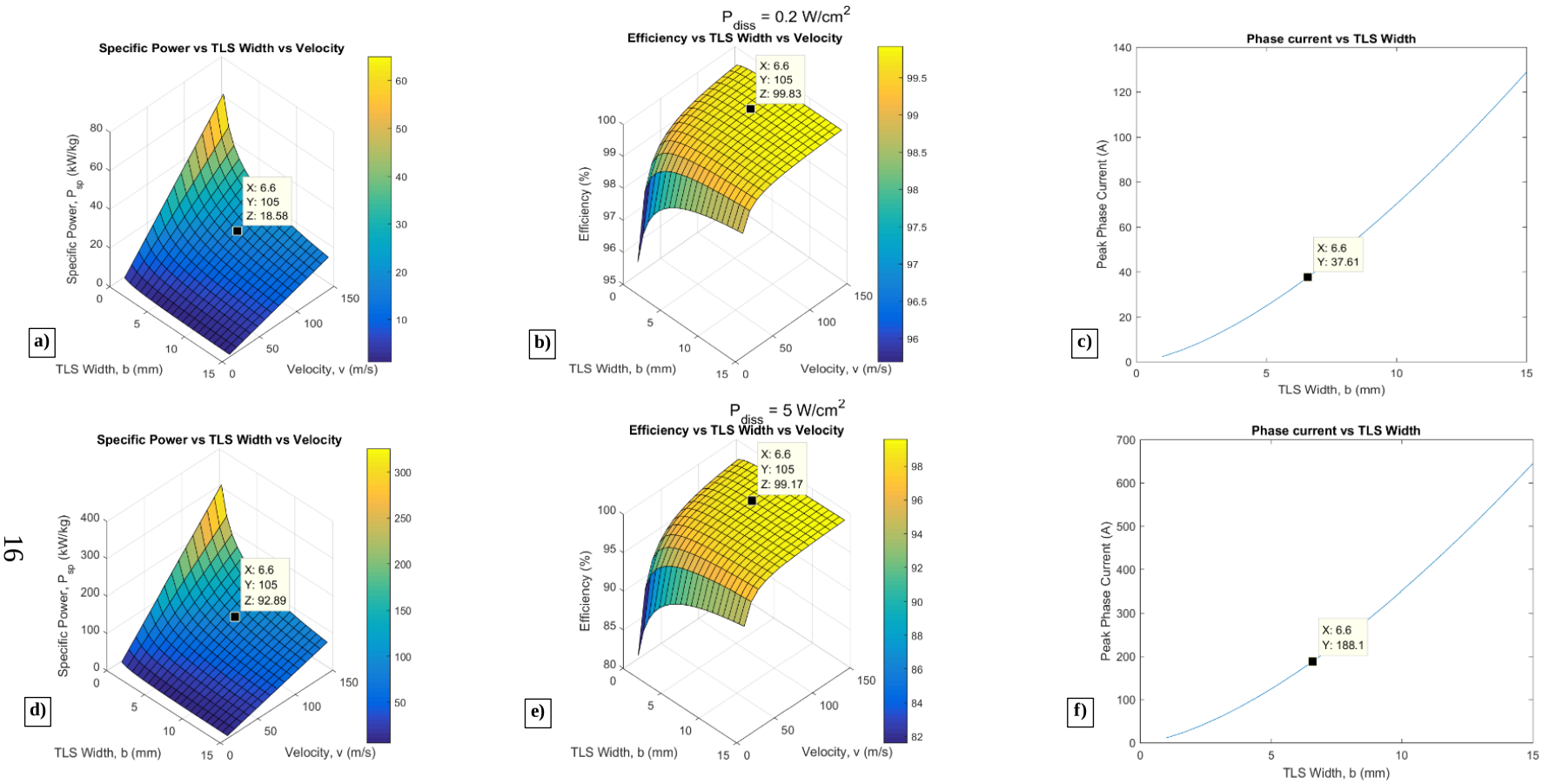


Figure 10: Using air cooling of TLS (dissipated power density of 0.2 W/cm$^2$) the **a)** specific power and **b)** efficiency are plotted for the TLS as they vary with TLS width and velocity. **c)** depicts the required peak phase current that must be supplied for a given TLS width and is independent of the velocity. Using moderate water cooling of the TLS (dissipated power density of 5 W/cm$^2$) the **d)** specific power and **e)** efficiency are plotted against the same variables. **f)** shows peak phase current vs TLS width.

The corresponding inverter size needed to supply this current can be calculated by solving for the peak phase current for a given dissipated power density, TLS width, blocking voltage, and switch length using equation (9), reproduced in Figure 11. The peak phase current for a TLS width of 6.6 mm that the inverter can supply is plotted in Figure 11. With a TLS width of 6.6 mm and a switch length of 3 mm and 6 mm, the current deliverable by this inverter is 130 A and 260 A, respectively. These calculations assumed a dissipated power density, or an effective cooling power density of the inverter of 50 W/cm$^2$ which is achievable using water cooling and low thermal resistance components. For this style inverter, using high thermal conductivity substrates is a must to keep thermal resistance at a minimum. A more thorough analysis of the thermal resistances in the inverter will be done in Chapter 2.

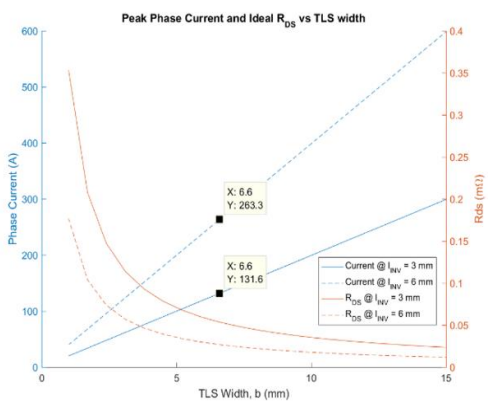


$$I_{\phi-RMS}^2 D \frac{2\left(5.93 \times 10^{-9}\, BV_{pp}^{2.5}\right)}{(bl_{inv})^2} + \frac{I_{\phi-RMS} V_D}{3bl_{inv}}(1-D) - \bar{P}_{diss_{INV}} = 0$$

| Parameter | Value | Units |
|---|---|---|
| Duty Cycle | 95 | % |
| Blocking Voltage | 20 | V |
| Dissipated Power Density | 50 | W/cm$^2$ |
| Inverter Length | 3 and 6 | mm |

Figure 11: Inverter peak phase current (blue) and corresponding $R_{DS}$ (orange) vs TLS width with parameters given in the chart to the right.

These plots and equations provide a parameter space for which a motor designer can start from to design a high-power density motor based on the cooling limitations of the application. It is important to note that these equations have been made independent of motor length and motor voltage. To incorporate these parameters into this analysis, one would need to relate the two using the velocity using the motor back EMF equation (2). Additionally, space will need to be allotted for cooling and wiring of the inverter to the motor, however it is understood that the added weight and volume should be small relative to the core numbers of the motor.

Furthermore, the switching, eddy current, and hysteresis losses have been left out of this analysis for simplicity, but with proper design techniques these losses can be kept to a minimum. These losses will further be addressed in Chapter 2.

# Chapter 2: Motor and Inverter Design

## 2.1 The Designed TLS Motor

The prototype rotary motor was built with cost, simplicity and manufacturability in mind while still demonstrating the impressive power density achievable by this topology. After considerable deliberation of design and research into materials, components, and manufacturing capabilities available, an in-runner motor with motor parameters shown in Table 3 were chosen. The CAD models of the fully assembled motor are shown in Figure 12. The stator laminations were laser cut from M19 Silicon Steel and stacked through outside suppliers; the rotor was machined from unlaminated 1117 carbon steel and epoxy heat shrink tubing was applied to retain the magnets to the rotor (Figure 13). The permanent magnets were repurposed from a previous experiment, made from N42 grade NdFeB magnets; a few broken magnets are shown laid around

Table 3: Designed In-runner Motor Parameters

| Parameter | Description | Value | Units |
|---|---|---|---|
| $N_{TLS}$ | Number of TLS Units (number of pole pairs) | 6 | - |
| b | TLS Width taken as $b = 2\pi R/N_{TLS}$ | 1.32 | cm |
| l | Motor stack length | 10 | cm |
| R | Effective radius (taken in the gap) | 1.26 | cm |
| $\bar{c}_b$ | Normalized TLS height | 1.0 | - |
| $t_{mag}$ | Magnet thickness | 2 | mm |
| $w_{mag}$ | Magnet width | 4 | mm |
| g | Air gap length | 0.88 | mm |
| $B_r$ | Magnet remanent flux density | 1.3 | T |
| $B_{gap}$ | Flux density achieved in gap ($B_{gap} = \frac{B_r t_{mag}}{t_{mag}+g}$) | 0.90 | T |
| K | Motor constant ($K = 2B_{gap}lR$) | 0.00228 | Nm/A |
| $Vol_{MOT}$ | Volume of stator and rotor with conductors and magnets | 102 | $cm^3$ |
| $m_{MOT}$ | Mass of stator and rotor with conductors and magnets | 0.76 | kg |
| $\rho_{MOT}$ | Averaged motor density | 7466 | $kg/m^3$ |
| $m_{TOTAL}$ | Total mass with motor, end caps, support components | 1.29 | kg |
| RPM | Maximum RPM (bearing limited) | 30000 | RPM |
| $R_\phi$ | Phase Resistance | 0.65 | mΩ |
| $L_\phi$ | Phase Inductance | 210 | nH |

the circumference of the rotor. The final assembled motor with machined end caps, motor support brackets, stator, rotor, windings, and rotary encoder are shown in Figure 14.

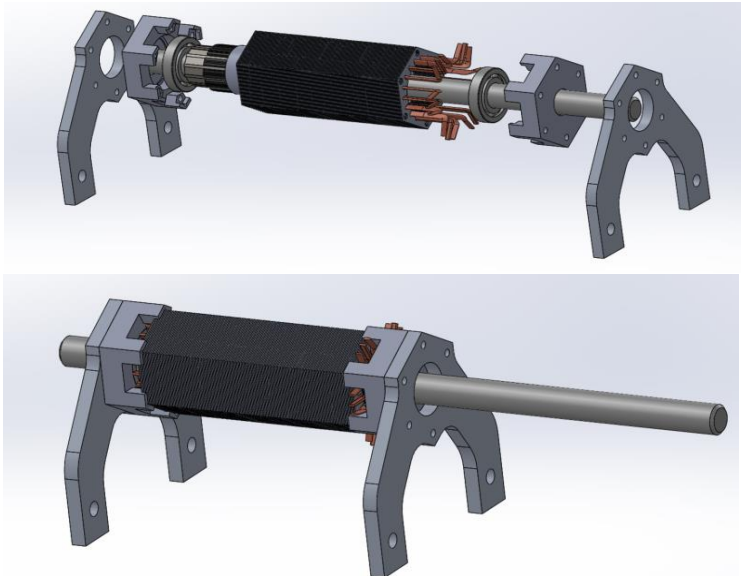

Figure 12: Exploded and assembled view of the rotary motor

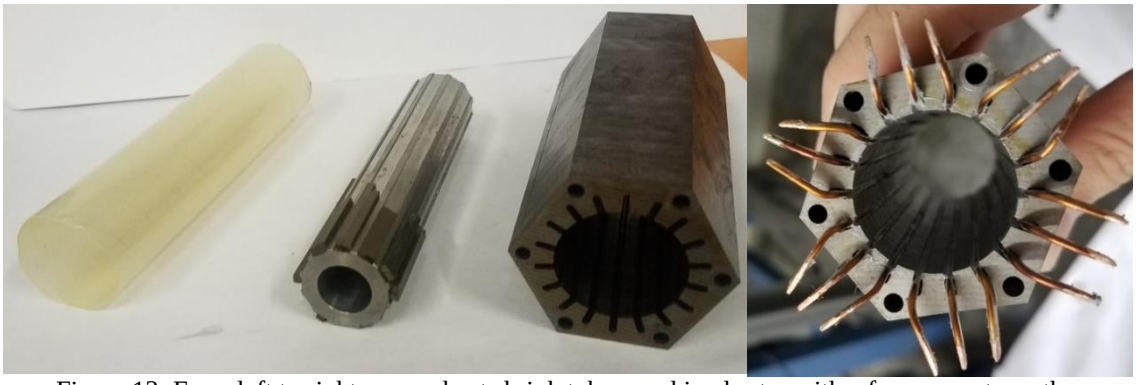

Figure 13: From left to right: epoxy heat shrink tube, machined rotor with a few magnets on the periphery, the assembled stator lamination stack, and the assembled stator with conductors

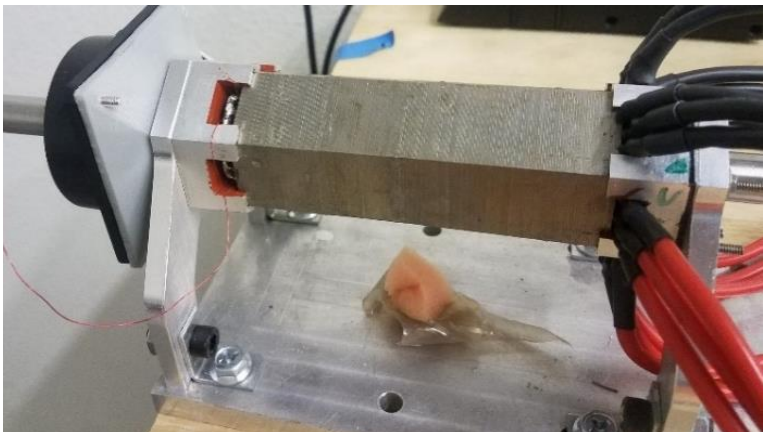

Figure 15: Fully assembled motor, with the encoder mounted to the shaft on the left and the fanout wires to the cooling plate on the right

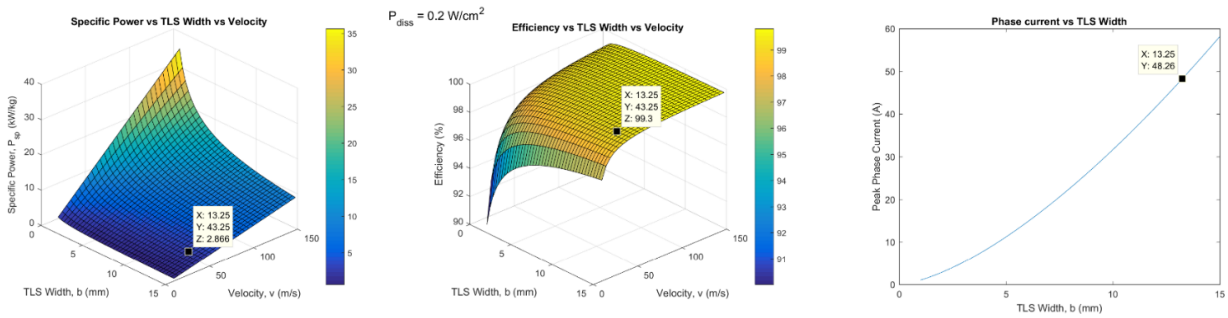


Figure 14: Specific power, efficiency, and phase current plots for the circular motor. The key values for this motor using air cooling is 3 kW/kg, 99.3% efficient, and a phase current of 48 A.

Figure 15 depicts the updated plots found in the previous chapter using these motor's geometries given in Table 3. With limited air cooling of this motor, the projected specific power would be ~ 3kW/kg at a surface velocity of 43 m/s (~32000 RPM) and a phase current of 48 A, which is by no means record breaking. To see what the motor is capable of with better cooling, Figure 16 shows plots of the specific power, efficiency and current as they vary with cooling power density and velocity for the fixed TLS width. While the prototype motor does not have a cooling system to remove this much power continuously, it can operate at these values for short periods of time to demonstrate the capabilities with proper cooling.

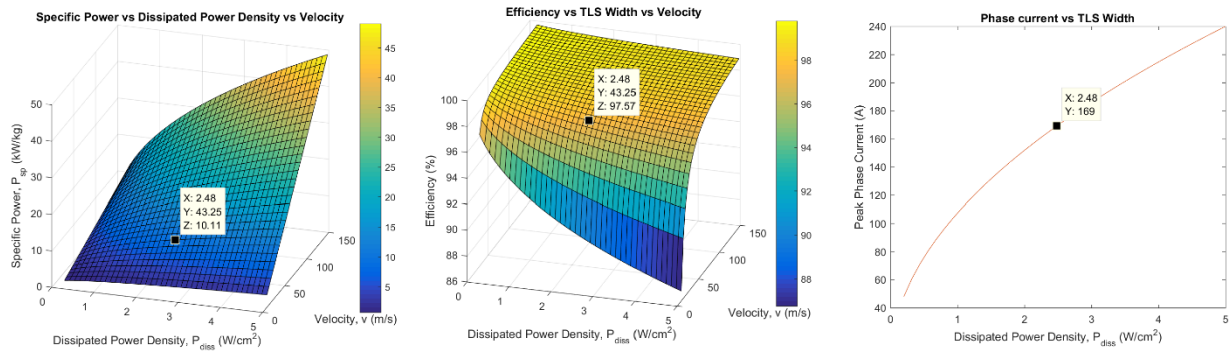


Figure 16: Specific power, efficiency, and phase current as they vary with dissipated power density and velocity using a TLS Width, $b = 13.2\ mm$

Now, the maximum specific power achievable for a cooling of 2.5 W/cm$^2$ is 10 kW/kg which is comparable to the highest specific powers of current electric motor technologies. The drawback for going to these higher specific powers of course is a decrease in the motor efficiency. However, because there are no turns in the motor, the phase resistance is still very low, so the efficiency is still quite high at reasonable surface velocities.

Aside from the cooling limits on the motor, the other factor to consider is the current capabilities of the inverter. The inverter must be able to deliver these phase currents to the motor; the designed inverter will be discussed in detail in the following section.

## 2.2 The Designed TLS Inverter

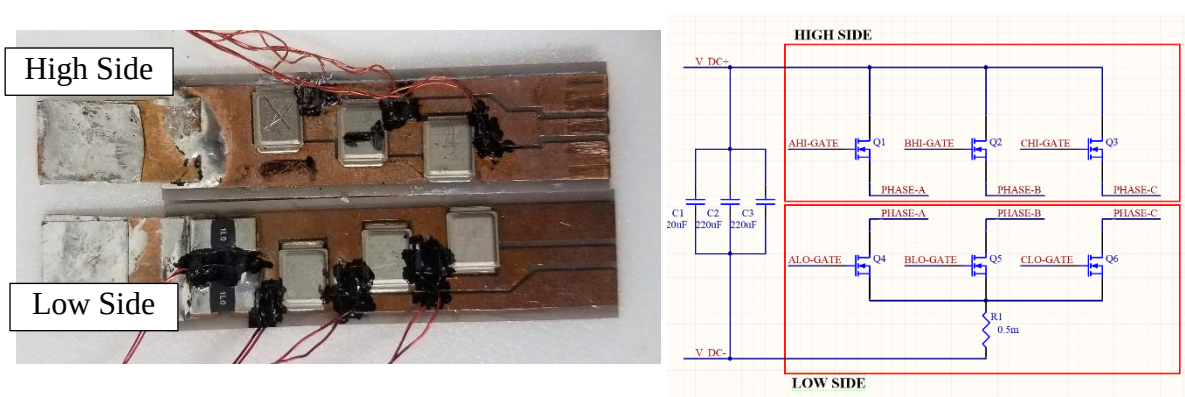


Figure 17: Custom three phase inverter circuits and circuit schematic

The inverter designed to match this motor was constructed on a Direct Bond Copper substrate (DBC) which is composed of three layers: .008” copper | .015” aluminum nitride (AlN) | .008” copper. This stack up allows for thick copper traces – relative to the typical .0014” copper clad FR4 boards used in PCBs – to pass the large currents needed for this motor. As mentioned in Chapter 1, the inverter circuit is split into the high side and low side switches and folded over the cooling plate; thus, two circuits were made for each TLS, and are pictured side by side with the schematic in Figure 17. The top layer of copper is etched in the typical manner of PCBs. The middle layer is used as an electrical insulator and heat conductor – the AlN ceramic has a thermal conductivity that is 43% that of copper, which is much better than most insulators. The bottom layer of the high/low side inverter is then attached to the cooling plate as shown in Figure 18, either via soldering directly or using thermal grease and adhesives. Using a simple thermal analysis calculation based on the stack up of this inverter, the resulting thermal resistance seen by the MOSFET is 3.2 $^{o}$C/W.  The cooling plate was custom built for a previous experiment and can cool up to 50 W/cm$^2$.

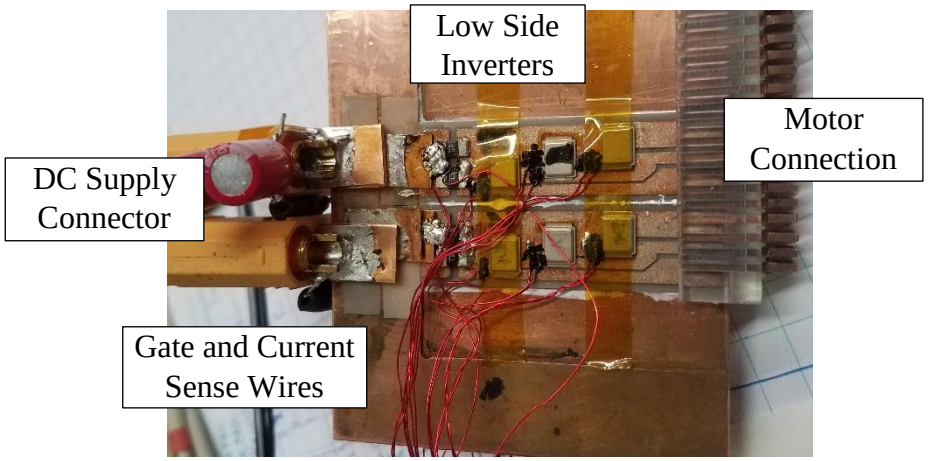


Figure 18: Two low side portions of the inverter are shown side by side mounted with thermal grease and kapton tape for initial testing.

The MOSFET used for this inverter is the IRL6283 from International Rectifier with an $R_{DS}$ of 0.5 mΩ and max blocking voltage of 20 V [13]. To limit the power losses and size of the

inverter, only a single current sense resistor was used to measure the current on the DC side of the inverter. As such, a rotary encoder was used for the sensored feedback control loop. The inverter parameters are given in Table 4.

Table 4: Designed Inverter Parameters

| Parameter | Description | Value | Units |
|---|---|---|---|
| $b$ | Inverter Width | 1.27 | cm |
| $l_{inv}$ | Total inverter length | 4.4 | cm |
| $A_{FET}$ | Area of the die of the MOSFET | 0.078 | $cm^2$ |
| $V_D$ | Diode voltage | 0.7 | V |
| $V_{DS}$ | Max drain to source voltage | 20 | V |
| $V_{GS}$ | Gate Voltage Applied | 12 | V |
| $t_{rise}$ | Device rise time | 160 | ns |
| $t_{fall}$ | Device fall time | 192 | ns |
| $R_{DS}$ | Drain to source resistance | 0.5 | mΩ |
| $f_{sw}$ | Switching Frequency | 64 | kHz |
| $R_{trace}$ | Total trace resistance per phase | ~1.3 | mΩ |
| $R_{CS}$ | Current sense resistor | 0.5 | mΩ |
| $C_{TOT}$ | Total capacitance per inverter | 660 | µF |
| $R_{ESR}$ | Total effective series resistance | 3.3 | mΩ |

These values can now be evaluated to calculate the max current achievable with this inverter for a given cooling power density and compare them to the ideal case presented previously. Take note that these values will be substantially lower than the ideal case because switching losses will be incorporated in the calculation and current MOSFET technology cannot reach the ideal $R_{DS}$ case. The switching losses are calculated by averaging the power dissipated during the total switching time (rise and fall) across a single duty cycle. The switching losses can be calculated as follows:

$$P_{sw} = V_{DC} I_{\phi-pk} f_{sw} \left(\frac{t_{rise}+t_{fall}}{2}\right) \tag{10}$$

Equation (10) can then be substituted back into equations (7) and (9) to account for the switching losses. Additionally, the designed inverter has slightly different geometry (the switches are staggered back along the length the inverter) compared to the simplified case shown in Figure 9. Since the TLS width is set, the cooling power density will instead be varied in equation (9) while solving for the phase current. Shown in Figure 19 is the maximum ideal inverter phase current compared to the designed inverter values, along with a dissipated power breakdown. The real inverter current capabilities are 38% those of the ideal inverter. This large discrepancy can be attributed to fact that the switching losses were not considered – if switching losses were ignored for the designed inverter, its current would be 66% of the ideal inverter. As seen from the breakdown, the switching losses contribute the most compared to the conduction and diode losses due to the long rise and fall times of this switch.  It is important to note that these are still first order approximations of the achievable current; further modeling will be done using LTSPICE for a more exact analysis.

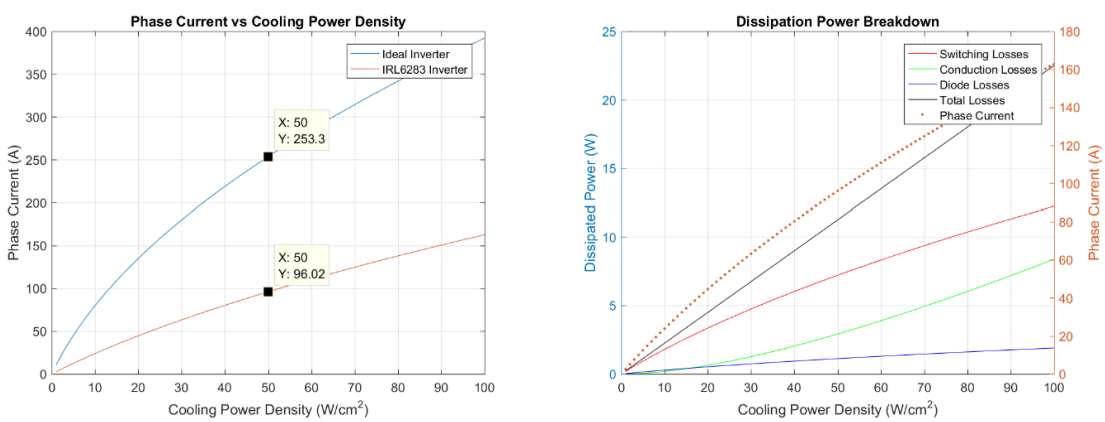


Figure 19: Left – Phase current as a function of the cooling power density on the inverter. From the selected datapoint, at a cooling of 50W/cm$^2$, the designed inverter can achieve 40% of the ideal inverter. The large discrepancy between these inverters is due to the large switching losses and higher on resistances in the designed inverter. Right – Total dissipated power breakdown in the inverter as a function of cooling power density. The solid lines represent the switching, conduction, diode, and total losses. The dotted orange line depicts the corresponding phase current in the inverter vs the cooling power density.

With a max current limitation of ~100A for the designed inverter, the max specific power can be recalculated to reflect this limitation. Looking at Figure 16, if the phase current is limited to 100A, the max cooling power density needed for the motor is 1 W/cm$^2$, the specific power is ~7 kW/kg, and the efficiency is 98%. While not record breaking, these are promising numbers for a first generation prototype.

### 2.3 2D Finite Element Analysis

To obtain a better approximation of the motor power density, more accurate calculations must be made with regards to the flux distribution in the motor. In particular, the achieved flux density in the air gap was approximated to be $B_{gap} = B_r \frac{t_{mag}}{t_{mag}+g}$ in Table 3, however this does not take into account the specific magnet geometry, spacing, or fringe effects. Additionally, the motor constant, which relates the back EMF to velocity and torque to current, does not consider the nuanced geometries of the stator and rotor. As such, the actual back EMF waveform is unknown and would likely lie somewhere between a sinusoid and a trapezoidal waveform. It is also helpful to perform this analysis to determine the maximum current limitations of the design before the steel saturates or the magnet is demagnetized.

The finite element analysis (FEA) was performed using FEMM, a free 2D FEA solver targeted towards static electromagnetic problems [14]. The software is straightforward so that complex geometries and materials can be input to the design space and solved. Additionally, the software has a scripting language (Lua) adapted for pre and post processing of the problem, making it easy to make slight modifications and record the results.

For this specific problem of determining the motor constant, two approaches can be taken: 1) place a static current in two of the phases, similar to the standard trapezoidal excitation scheme, and step the rotor angle over a full electrical rotation while measuring the torque

produced, or 2) measure the flux linkage in a single conductor while stepping through a full electrical rotation and calculate the back EMF/motor constant that results from it using Lenz' Law. For simplicity, the first approach was taken.

A positive current of 100 A was put into phase B and corresponding negative current was put into phase C. The rotor position was set to an arbitrary angle relative to the stator windings and stepped through a full electrical rotation, taking the torque at each location using Maxwell's stress tensor calculation, provided by FEMM. Figure 21 shows a color map of the flux density in the motor during one of these steps. The legend on the right shows that even at essentially 100 A per TLS, neither the magnets or the stator is close to demagnetization or saturation. Figure 20 shows the measured torque at 100 A/TLS at each step as well as a zoomed in view of the peak torque region, yielding a motor constant of .001911 Nm/A per TLS or an effective magnetic flux density of .76, which is 16 % less than what was expected. The lower peak magnetic flux density for this design is likely due to the thinner magnets used (in the radial direction) relative to the total motor thickness in the radial direction. With this information, we could expect a 16% decrease in the expected output power of the motor. The more sinusoidal torque waveform in the plot is because this motor has no windings which spread across the stator. Thus, the three

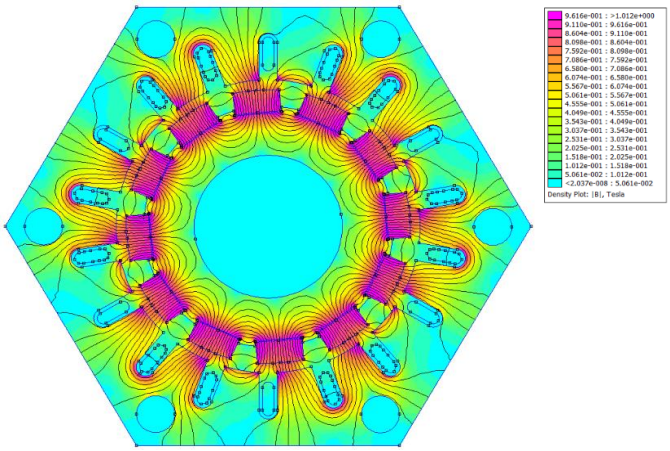


Figure 20: FEA output of the flux density plot with 100 A in Phases B and C

conductors will all have a small peak range for the maximum flux linkage that will reduce in a smooth sinusoidal fashion seen below.

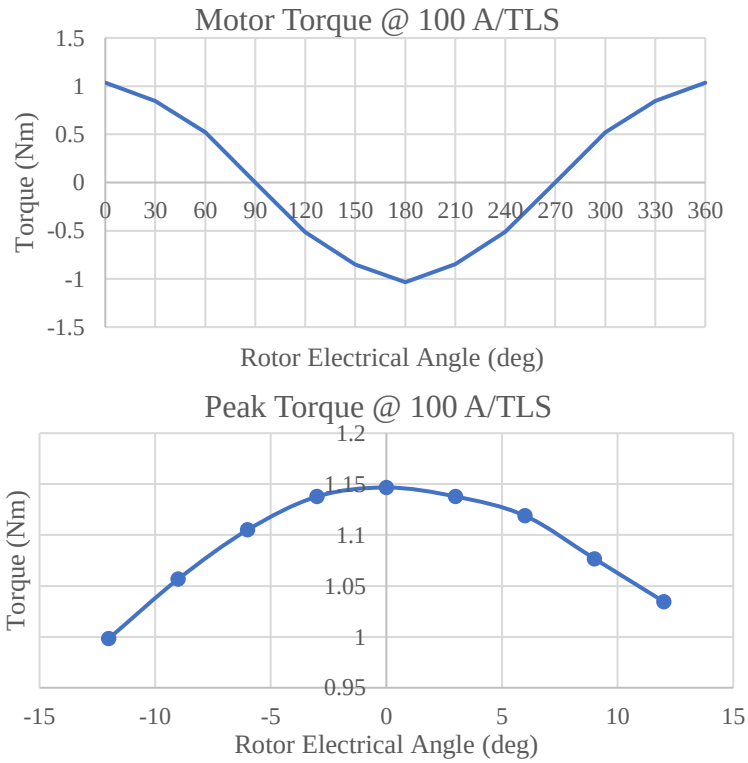


Figure 21: Top – measured torque output at 100 A/TLS across a full electrical period. Bottom – peak torque output taken over the optimal rotor electrical angle. The flux coupled into the stator is sinusoidal rather than trapezoidal.

## 2.4 Eddy Current and Hysteresis Losses

Eddy currents are currents generated in the stator as a result from the changing magnetic field produced by the rotating magnets in the rotor. The changing flux with respect to time induces a voltage and circulating current in the stator which creates a magnetic field that opposes the rotating magnetic field as seen in Figure 22. This analysis uses the derivation detailed in [15] for low frequency operation, which neglects the skin effect in the lamination. The derivation starts with Faraday's law (change in flux over time yields a voltage) and assumes the flux density to be uniform over a cross sectional area of a single stator lamination. After considering the geometry of a lamination, the electric field in the stator is found for a given frequency and peak

magnetic flux density. The eddy current density is calculated by multiplying the electric field by the conductivity of the steel, which can then be used to find the eddy current power loss per unit mass – see equation (11).

$$P_{Eddy} = \frac{\sigma B_{gap}^2 (2\pi f)^2 t_{lam}^2}{24\rho} \tag{11}$$

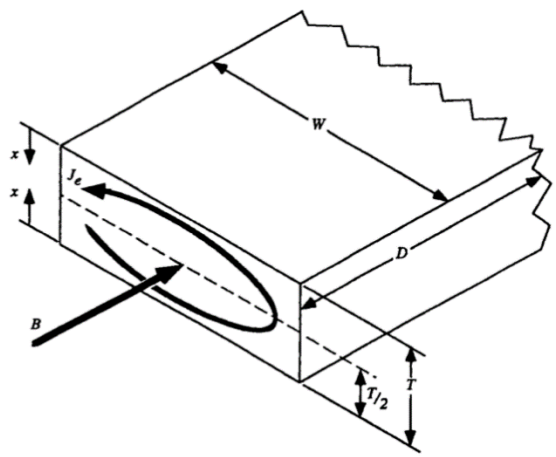


Figure 22: Resultant eddy current, $J_e$, in a single lamination from an applied magnetic flux density, $B$. Using the right hand rule, the corresponding field produced by the eddy current acts to oppose the applied field [15].

Additionally, hysteresis losses should be considered. This energy loss occurs because there is a certain minimum energy required to orient the magnetic domains within the stator to change from one direction to another. This is referred to as the magnetic hysteresis loop and is shown by plotting the path the material takes during changing magnetic flux densities – see Figure 23. The area under the loop represents the energy lost as heat over each cycle and can be approximated by equation (12), where $H_c$ is the coercive force of the steel and $\rho_{steel}$ is the density of the steel [15].

$$P_H = \frac{4B_{gap}H_c f}{\rho_{steel}} \tag{12}$$

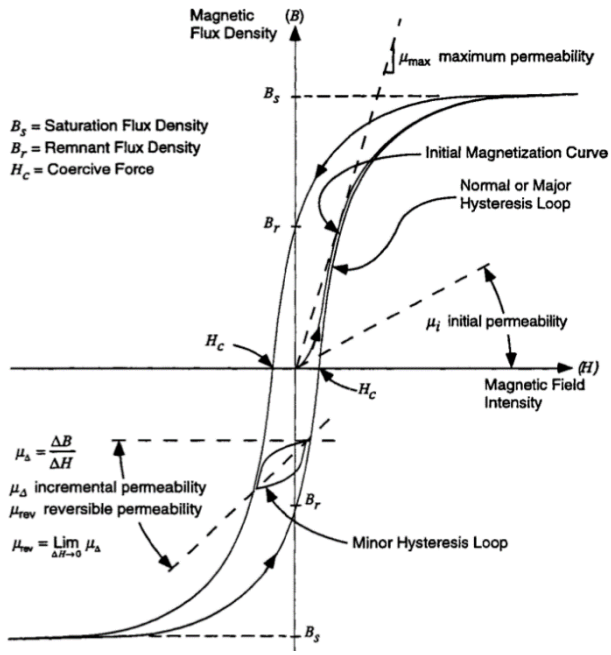


Figure 23: Typical magnetic hysteresis loop for soft magnetic materials [15].

Specific steel alloys, typically known as electrical steel, have been developed with very thin hysteresis loops and very large resistivities to minimize the hysteresis and eddy current losses. For this application, M19 silicon steel with a lamination thickness of 0.635 mm was chosen for its cost effectiveness at moderate performance.

The following graph, given in Figure 24, show the power losses due to eddy currents and hysteresis losses assuming the peak magnetic flux density is set by the permanent magnets, stator mass of .471 kg, and the relevant parameters for M19 silicon steel taken from [15]. The eddy current losses are much larger than the hysteresis losses because they vary with flux density, thickness, and frequency squared. For this application, the frequency is larger because there are six pole pairs – the electrical frequency is six times the mechanical frequency – and the lamination thickness is on the larger side. The resulting power loss from eddy currents for this motor at 22000 RPM is 226.8 W, which will limit the mechanical power output of this motor.

However, it is understood that this is a prototype motor for demonstration of the concept; the lamination thickness could easily be made much thinner to improve these numbers. These eddy currents could be seen as a real load on the motor and will be viewed as such in Chapter 3.

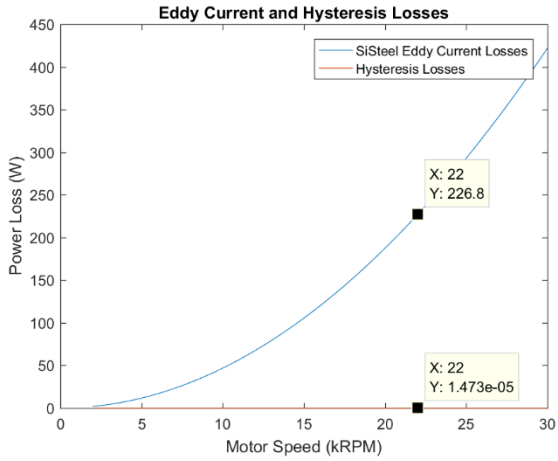


Figure 24: Eddy current and hysteresis losses versus motor speed

## 2.5 SPICE Analysis

To better model the circuit performance of the inverter and motor, the system was built in LTSPICE. The main goals for this analysis was to measure the total losses in the inverter per phase and the resistive losses in the motor per phase. A simple motor unit was modeled using a resistor, inductor, and sinusoidal voltage source for each phase of the TLS to match the waveforms found in the previous section. The SPICE model for the IRL6283 was supplied by International Rectifier. The gate driver was constructed from ideal voltage sources and switches,

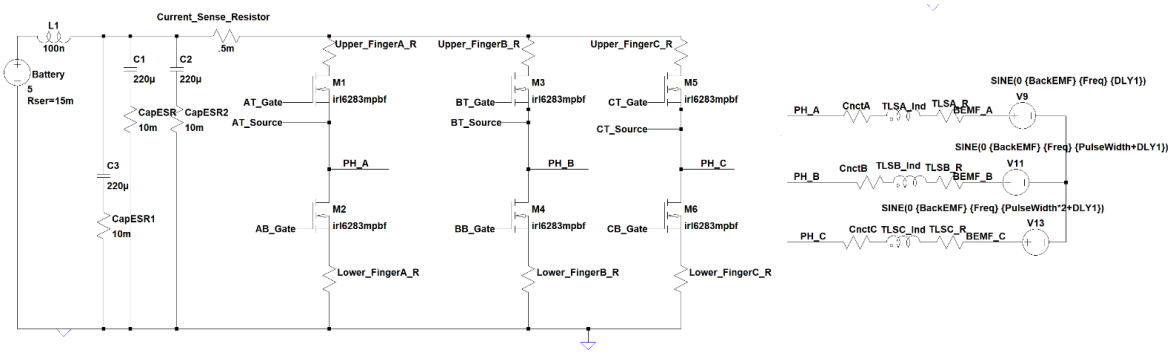


Figure 25: Inverter and Motor Circuit

but the gate resistances were chosen to match the output capabilities of the gate driver selected for this application. To generate the proper trapezoidal signals, a square wave generator was used in combination with logic gates and delays to sync the back EMF to the current waveforms. The main circuit is shown in Figure 25. To match this circuit to the experiment detailed in the following chapter, the RPM was chosen to be 16500 RPM and a DC supply voltage of 5V. Figure 26 shows a single phase trapezoidal current in phase with the line to neutral back EMF waveform.

The resulting power losses are tabulated in Table 5 and compared to the first order analysis done in the previous section applied to these parameters. As seen from the table, the rough analysis was within 10 % of the SPICE results which confirms the analytical approach taken for this problem.

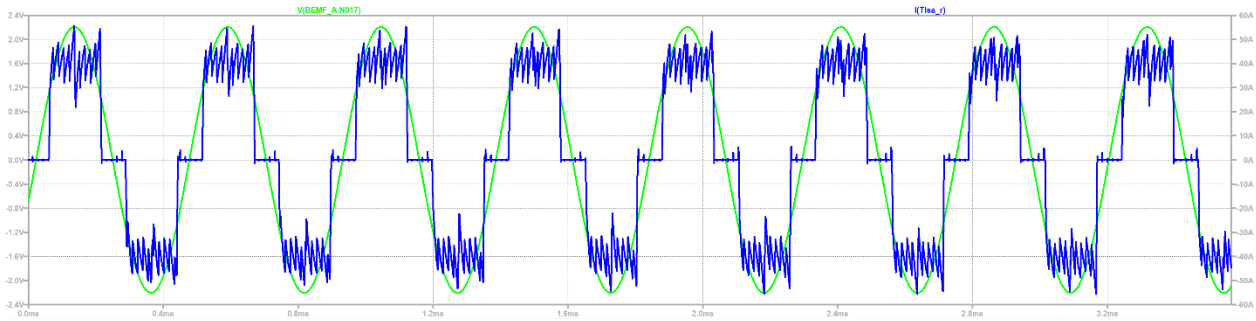


Figure 26: Phase voltage and current waveforms @ 22000 RPM, 90% Duty and 5V DC Supply. The resulting RMS phase voltage is 1.56 V and current is 33.3A. The peak current can be approximated to 40.8 A.

Table 5: Inverter and Motor losses

| | **Description** | **SPICE Analysis (W)** | **First Order Analysis (W)** |
|---|---|---|---|
| $P_{HIGH\text{-}SIDE}$ | Averaged high side switch losses in phase A | .843 | 1.03 |
| $P_{LOW\text{-}SIDE}$ | Averaged low side switch losses in phase A | 1.232 | 1.22 |
| $P_{TOTAL}$ | Total losses in the switches per phase | 2.1 | 2.25 |
| $P_{RESMOT}$ | Resistive losses in the motor | 2.16 | 2.2 |

# Chapter 3: Experimental Results

### 3.1 Experimental Setup

The experimental setup, shown in Figure 27, consists of two of the designed motors mounted on the same shaft. One acts as a motor, and the other as a generator. The motor is powered from multiple 5V 200A power supply units connected in parallel. Motor conductors are fanned out with 12 AWG wire to the cooling plate, which has the inverters mounted with thermal grease and super glue. The custom built cooling plate is pumped with cold water from a water pump located below at the rated pressures and flow rates to achieve up to 50 W/cm$^2$ cooling (Figure 28). The connector between the cooling plate and the motor wires were specifically designed for a previous linear actuator experiment and repurposed for this application. The gate driver circuits, also repurposed from a past experiment, take in the control signals from the microcontroller and drive the inverters sitting on the cooling plate via twisted pair magnet wire – see Figure 30. Current sensors are connected to the current sense resistor on each low side of the inverters and are monitored on the oscilloscope – these signals are just used for monitoring and are not part of the feedback control loop. The encoder is mounted on the end of one of the stators and its signal is fed into the microcontroller for speed control. Thermocouples are mounted onto a few of the MOSFETs to monitor temperatures on the switches to ensure proper thermal performance. Motor temperature was measured periodically using an IR temperature sensor.

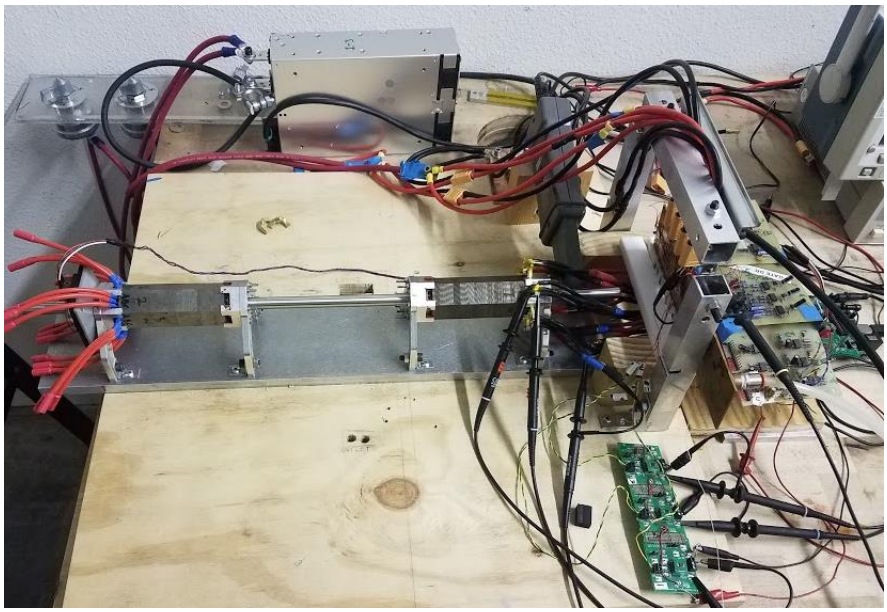

Figure 27: Overview of the motor experiment setup

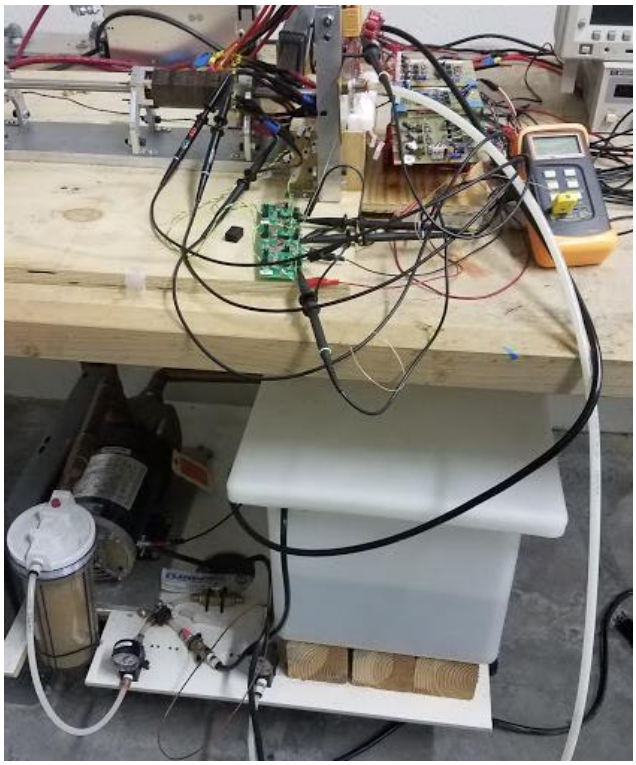

Figure 28: Cold water pump with tank, valves and tubing leading up to the cooling plate

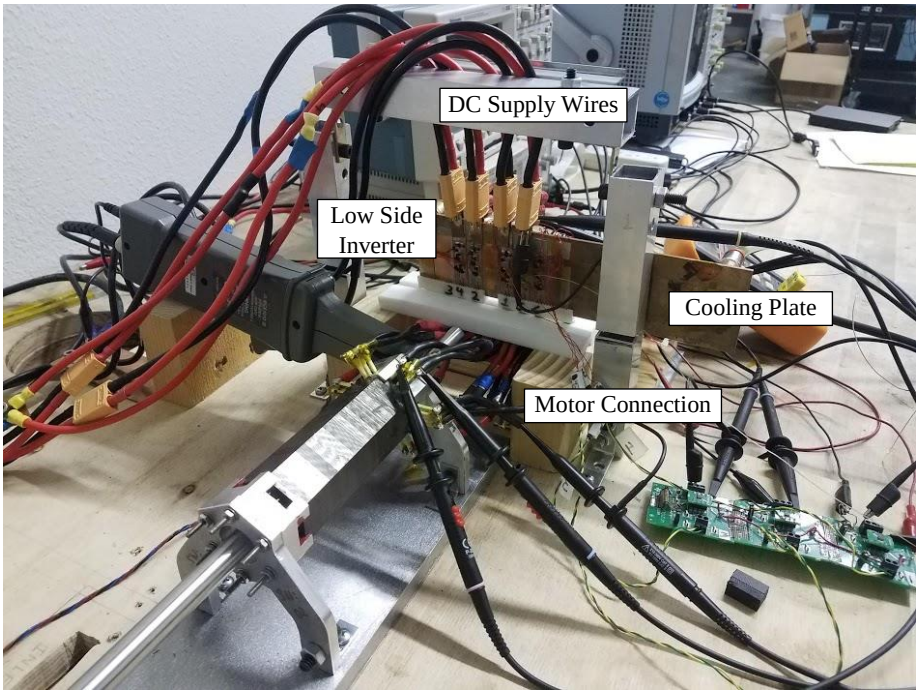


Figure 29: Motor connection to the cooling plate with the low side of the inverters showing. The DC supply wires are coming in from the top and connected to the other side of the cooling plate using XT90 connectors.

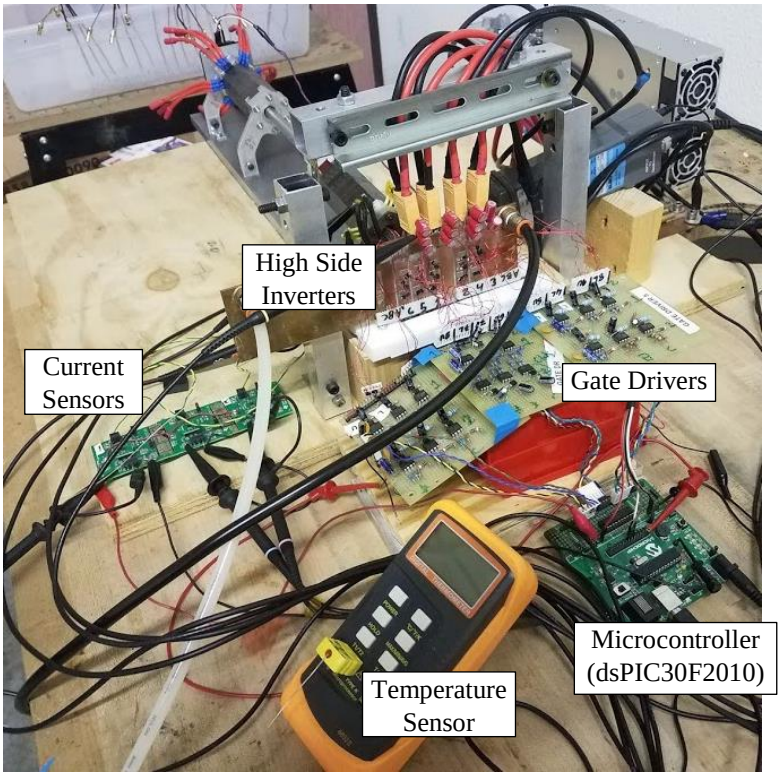


Figure 30: View of the gate driver connection to the inverters via magnet wire and the current sense amplifiers to the left. In this experiment, only four inverters were connected to the motor leaving two TLSs undriven.

## 3.2 Motor Control System

The focus of this thesis is primarily on the motor and inverter design implementation; as such the motor control system was kept simple and will be discussed briefly. For this motor, a sensored 120° trapezoidal commutation method was chosen to drive the motor as mentioned in Chapter 1. The control system diagram is shown in Figure 31 using the dsPIC30F2010 microcontroller and a rotary encoder as position feedback. A simple PID controller was coded into the microcontroller and the parameters were adjusted experimentally. For the following experiments, only the proportional portion of the controller was used. Both loops were updated at a rate of 9.2 kHz. This control system was simple and effective for testing and debugging of the motor and inverter.

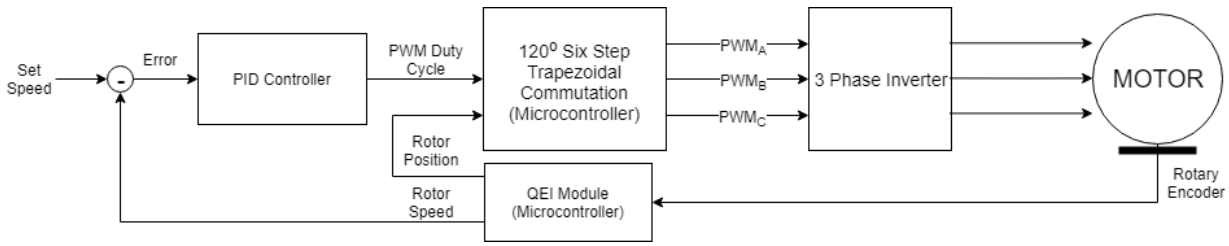


Figure 31: Motor Control Block Diagram. Both loops ran at 9.2 kHz.

## 3.3 Experimental Results

There were two tests performed to analyze the performance of this system. The first experiment was performed to demonstrate capabilities of the motor under no load, operated at close to the maximum RPM to demonstrate the higher velocities capable of the motor. The second experiment was aimed at demonstrating the current capabilities of the inverter which was done at lower speeds and higher currents. In the results section, the combined achieved values of these two experiments will be compared to the projected analytical calculations.

The first experiment was run at 22000 RPM, driving one motor with the generator left disconnected from a load. The main losses that the motor had to drive were eddy current losses and frictional losses. As detailed in Chapter 2, the eddy current losses become quite significant at very high velocities. The resulting metrics from the experiment are documented in Table 6 and Figure 32. Channel 1 (yellow) shows the line to line A-C BEMF voltage waveform which is rather sinusoidal. Channel 4 (green) shows the phase A current which lags the line to line phase voltage by 30$^{o}$ so that it is actually in phase with the line to neutral voltage. As seen from the table, the calculated values from FEMM and LTSPICE are very close to measured voltages and currents in the experiment. Despite no mechanical load on the rotor, the measured output motor power is quite high (529 W) which is needed to drive the eddy current losses and frictional losses.

Table 6: High RPM Experimental Results

| **Parameter** | **FEMM/SPICE** | **Measured Results** | **Units** |
|---|---|---|---|
| Achieved RPM | 22000 | 21930 | RPM |
| Duty Cycle | 90 | 90 | % |
| $V_{LL}$ BEMF RMS | 2.70 | 2.44 | V |
| $V_{LL}$ BEMF Peak | 3.82 | 3.45 | V |
| $V_{LN}$ BEMF RMS | 1.56 | 1.41 | V |
| $V_{LN}$ BEMF Peak | 2.21 | 1.99 | V |
| Effective B | 0.76 | 0.69 | T |
| Motor Constant | 0.00191 | 0.00173 | Nm/A |
| Phase Current RMS | 33.32 | 32.80 | A |
| Phase Current (Averaged Peak) | 40.81 | 40.17 | A |
| Motor Power Out per TLS | 147.9 | 132.3 | W |
| Total Motor Power out | 592 | 529 | W |
| Average DC Voltage | 4.4 | 4.3 | V |
| DC Power Per TLS | 163 | 173 | W |
| DC Power | 653 | 691 | W |
| Estimated Eddy Current Loss | 454 | 454 | W |
| Remaining Frictional Loss | | 75.4 | W |
| Total Frictional Torque | | 0.033 | Nm |

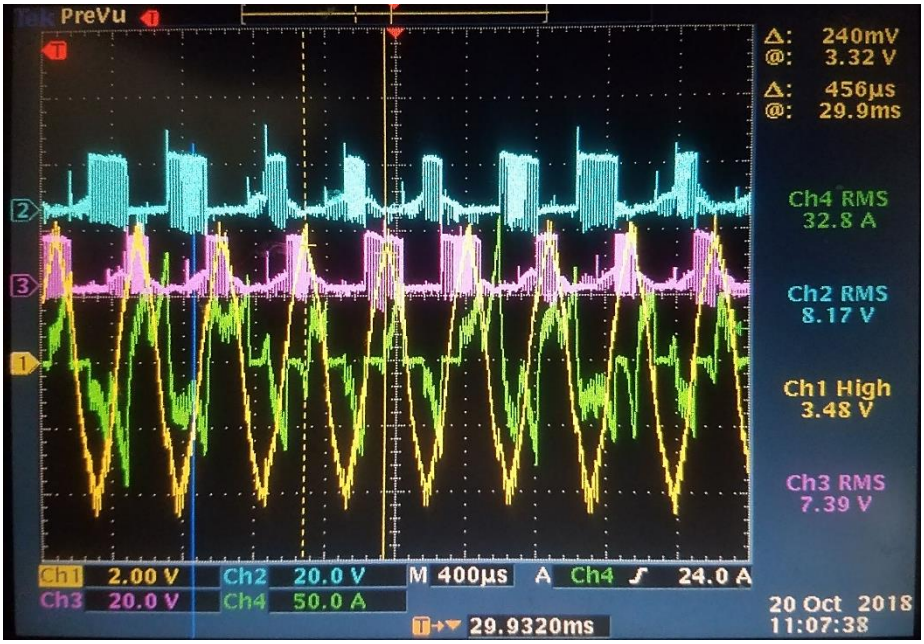


Figure 32: Oscilloscope Capture of Motor Waveforms. Ch. 1 - Motor BEMF from phase A-C. Ch 2,3 - Driven Phase C, A - Ground voltages, Ch. 4 - Phase A current

Additionally, the BEMF and corresponding B for the measured motor is 10 % lower than the expected values which is likely due to the increased total motor temperature resulting in a decrease in the magnetic flux density of the permanent magnets. This increase in motor temperature was due largely to the eddy current losses which heated the motor considerably during running. The measured change in temperature on the motor matched the expected results from the specific heat capacity equation for the time ran.

The second experiment was performed to show the current capabilities of the motor - inverter under a moderate load. The load connected to the generator is a custom built resistor bank made of iron wire operated for a short period of time, pictured in Figure 33. The voltage and current waveforms are measured directly on a single TLS to measure the output power, which is then extrapolated to the remaining six circuits.

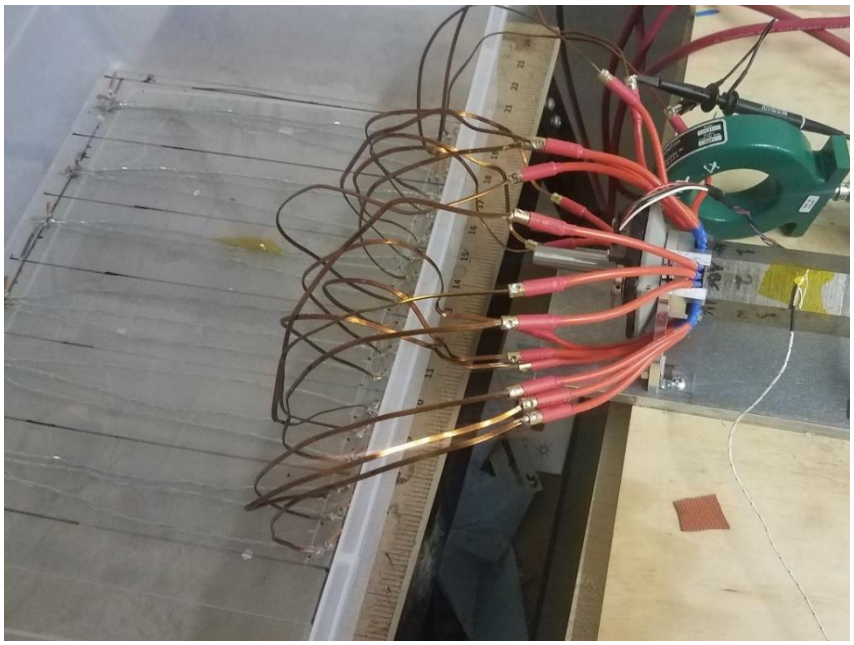

Figure 33: Three phase resistor bank connected to the generator side.

The resulting phase current and phase voltage waveforms for the motor and generator are shown in Figure 34. Note that the BEMF voltage on the generator (Ch. 4) is lower than the motor BEMF voltage – this is due to difficulties in the magnet layout on the rotor of the generator unit. The experimental results are detailed in Table 7. The effective $B$ in the gap matched the expected results from FEMM of 0.75T which is within 2 % of the modeled value. The achieved continuous DC current passed through a single inverter was 78.5 A with a MOSFET temperature of 55 $^{o}$C; which is close to the 96.2 A given in the previous chapter using 50 W/cm$^2$. Furthermore, this achieved current of 87.2 A is not at the cooling limit of the inverter since the switch temperature remained at 55 $^{o}$C. The maximum capabilities of the switch would likely be closer to or even more than the predicted value of 96 A since there was an extra 95 $^{o}$C before reaching the switch temperature limit of 150 $^{o}$C. The measured motor apparent power was 738 W which can be broken down into its output power on the generator side, eddy current losses, frictional losses, and angle between the phase current and phase voltage.

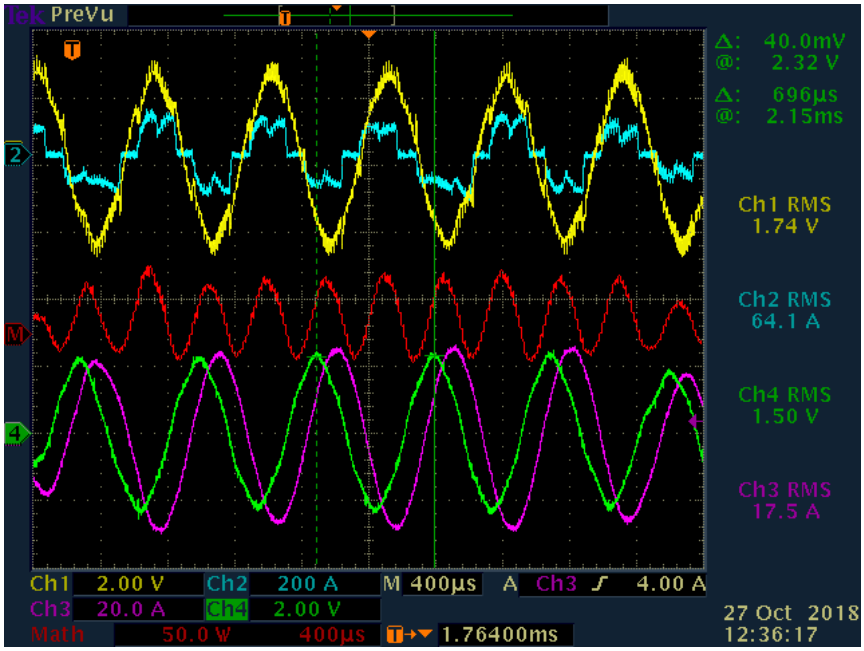


Figure 34: Oscilloscope capture of the second experiment. Ch. 1 - Motor line to line voltage, Ch. 2 - Motor phase current, Ch.3 Generator phase current, Ch. 4 Generator line to line voltage.

Table 7: High Current Experiment Results

| Parameter | Motor | Generator | Units |
|---|---|---|---|
| Achieved RPM | 14270 | 14270 | RPM |
| Duty Cycle | 86 | - | % |
| VL-N BEMF RMS | 1.00 | 0.87 | V |
| VL-N BEMF Peak | 1.42 | 1.22 | V |
| Effective B | 0.75 | 0.65 | T |
| Phase Current RMS | 64.1 | 17.5 | A |
| Phase Current (Averaged Peak) | 78.5 | 24.7 | A |
| Apparent Power Out | 737.9 | 272.8 | W |
| Inverter Temperature | 55 | | ºC |

## 3.4 Results

The maximum achieved results from these experiments are tabulated in Table 8. If the two experiments were combined – higher RPM BEMF of 1.99 V (or 2.21 V without heating) achieved at a larger phase current (96 A) – the resulting power per TLS would be 287 W and the specific power would be 2.37 kW/kg. This result, while still lower than the projected specific power detailed in Chapter 1, is close to the expected specific power at this motor's configuration

of 3.3 kW/kg at 29 m/s or 22000 RPM, highlighted in Figure 35. With a larger voltage source and larger load (through the use of a dynamometer or larger electrical load for the generator), the limits of this motor could be explored further. A very reasonable extrapolation of these results by increasing the inverter current to the projected limit of 100 A and using 30000 RPM, would place the specific power of this motor at 3.9 kW/kg. Overall, this specific motor's performance falls within the expected range of values shown by the simulations and analysis and should be capable of scaling up to higher specific powers.

Table 8: Combined Experimental Results

| **Parameter** | **High Current** | **High RPM** | **Units** |
|---|---|---|---|
| RPM | 14100 | 22000 | RPM |
| $V_{LN-pk}$ | 1 | 2.21 | V |
| $I_{\phi_{pk}}$ | 78.5 | 40.8 | A |
| Power | 130 | 149 | W |
| Combined Power | 287 | | W |
| 6 TLS Power | 1722 | | W |
| Specific Power (Motor Mass) | 2.37 | | kW/kg |
| Specific Power @ 30kRPM | 3.9 | | kW/kg |

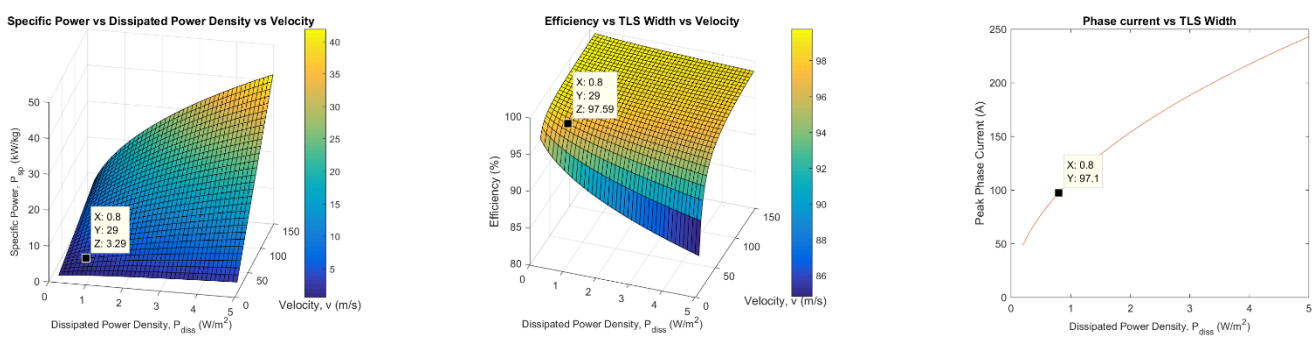


Figure 35: Extrapolated results of the constructed motor highlighted by the data points on the theoretical analysis plots.

### 3.5 Future Work

This project focused on using inexpensive and quick prototyping methods to rapidly construct a novel functional motor design. The near term future goals would be to push the current limitations on the inverter by making slight modifications to the generator load to run the motor at a lower RPM and higher current. Mechanical modifications should also be made to reduce frictional losses and quirks with the construction.

For the next prototype design, moving to a smaller TLS width, both on the inverter and on the motor side is absolutely necessary. To achieve these goals, the inverter should be designed into a smaller form factor using better switches. Some preliminary analysis has shown that moving to GaN switches could offer a larger improvement on current density in the inverter because they have 1) much faster switching speeds, and 2) can be operated in both directions, reducing the switching and diode losses in the circuit [16]. This improvement could yield much smaller inverters, likely on the scale of 6 mm or less. Additional work also needs to be done on selecting smaller gate drivers and microcontrollers to control these switches. Ideally, the gate drivers and microcontrollers could be confined to the very same width on a portion behind the inverters, making the entire system and extremely reliable. The cooling plate would also need to be revamped to accommodate this set and designed to lay the inverters along the periphery of the motor. Lastly, more sophisticated control techniques could be implemented such as field oriented control or even the use of TLS's as part of an active magnetic bearing system.

For the motor itself, the motor geometry – magnet dimensions, slot width, slot depth, rotor/stator thicknesses – could be further analyzed using FEA for different configurations to determine which geometry produces the largest magnetic flux density in the gap without

saturating the iron. Also, analysis on the cogging torque of the motor could be examined for more critical load requirements.

Furthermore, to make this topology more approachable to industry, a DC-DC converter should be designed that would take higher voltage – around 100 - 500 V – and drop it down to the range of 20 V to be used by the motor. It is envisioned that each of these converters would provide power to a few TLS – inverter sets in parallel to improve reliability and reduce the current requirements of any single converter. This could be done in multiple stages as well, depending on the voltage level requirements of the system as seen in Figure 36.

The capacitors for this motor have been selected using a simple DC-link capacitor sizing equation and increased by a factor of 2-3 to reduce the effects of self-heating and their effective series resistance. Further analysis and research into high power density battery/capacitor technology needs to be done to minimize the volume of these energy storage units and ensure they do not become a limiting factor in this design.

An overall system overview for a larger scale motor of this topology for aerial vehicle applications is shown in Figure 36. The a few of the future works mentioned in this section are detailed throughout the diagram.

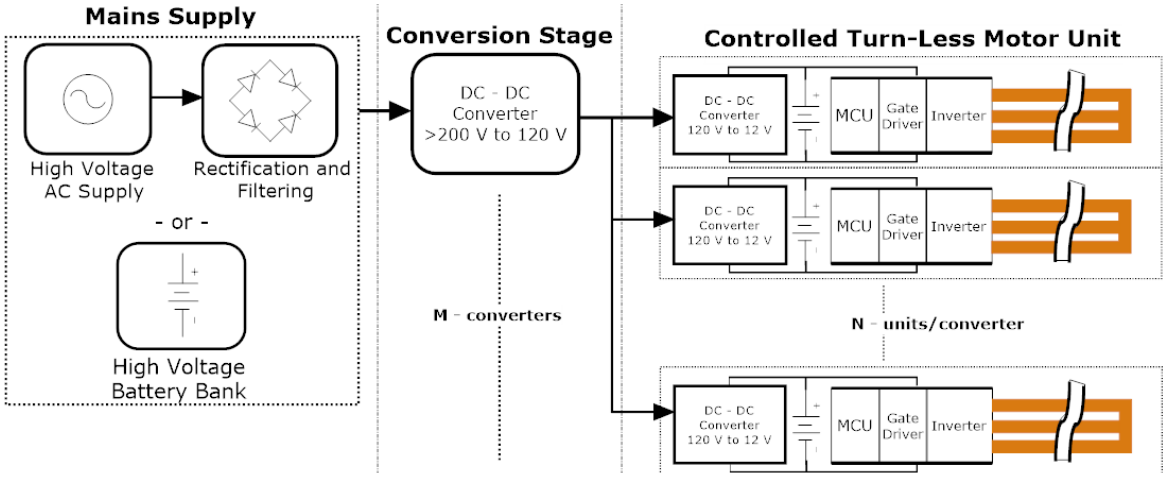


Figure 36: System overview of many TLS units paralleled with dedicated gate drivers, microcontrollers, and DC-DC converters connected to a larger DC-DC converter stage. This system would be meant to drive very high power motor applications.

# Conclusion

This thesis has demonstrated a novel topology of the standard brushless DC permanent magnet motor and the experimental work done on the motor. The primary focus was to present a power density analysis on a basic motor unit to show the motivations behind moving towards a turn-less motor unit. The plots and equations given in chapter one are used to show what knobs a motor designer has to construct the system described and to adapt this arrangement into requirements set forth by the application. Chapter two details the design and analysis using FEMM and LTSPICE on the constructed motor and inverter set which is used to predict their performances and compare them to the first order analytical results in chapter one. Chapter three details and summarized the experimental results and compares them back to the updated analysis done in the previous chapter. Overall, this motor analysis shows great promise for this motor topology and leaves much more work to be done to investigate further.

# Appendix A: Motor Analysis Derivations

The remaining derivations not explicitly shown in the thesis document prior are the motor efficiency and the ideal specific on resistance of the MOSFET, both of which will be detailed below.

**Motor Efficiency:**

This calculation is based solely on the expected motor output power and the resistive losses in the motor. It does not consider eddy current or hysteresis losses. To calculate the efficiency using previous equations, the output motor power is compared to the resistive losses, denoted as $Y$:

$$Y = \frac{\bar{P}}{\bar{P}_{diss_{TLS}}} = \frac{\frac{Bv2I_{\phi-pk}}{\bar{c}_b b^2}}{\frac{2{I_{\phi-pk}}^2\rho_{Cu}}{b^3\bar{A}_{cu}}} = \frac{I_{\phi-pk}\rho_{cu}}{\bar{A}_{cu}b^2Bv}$$

The cooling power density is then substituted in for the phase current to be consistent with the rest of the cooling power limited equations.

$$Y = \frac{1}{Bv}\left(\frac{\bar{P}_{diss_{MOT}}\rho_{cu}}{2b\bar{A}_{cu}}\right)^{\frac{1}{2}}$$

Typical efficiency is given as motor output power over the total input power, while Y is expressed as output power over resistive losses. The following equation shows the conversion between the two:

$$Eff = \frac{1}{1+Y}$$

**Motor Power Calculations with Trapezoidal Currents:**

Most of the power calculations used here were slightly different than the standard three phase power calculations since we are injecting a trapezoidal phase current. To derive the proper power, we integrated a sinusoidal voltage waveform with a trapezoidal current waveform and divided over a period. The resultant equation, which has been used in most of the calculations presented is as follows:

$$P = \frac{3\sqrt{3}}{\pi} V_{\phi} I_{\phi pk}$$

Additionally, the peak phase current varies from the rms current by the following relation:

$$I_{\phi rms} = \sqrt{\frac{2}{3}}\, I_{\phi pk}$$

**MOSFET Specific Ideal On-Resistance:**

The ideal on resistance for the MOSFET was derived from [12]. This derivation calculates the resistance of the ideal drift region in the MOSFET assuming an abrupt junction profile, yielding a triangular electric field distribution shown in Figure 37.

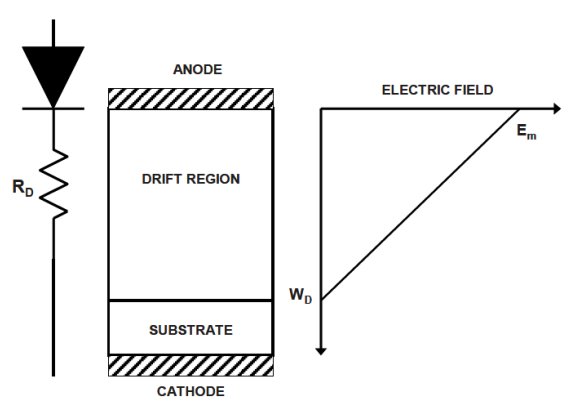


Figure 37: Ideal drift region of an abrupt junction (high to low doping concentration) as in the case of a MOSFET and the associated electric field [12].

The corresponding specific on resistance is given by:

$$R_{on,sp} = \left(\frac{W_D}{q\mu_n N_D}\right)$$

Where $W_D$ is the maximum depletion width of the drift region under the critical electric field, q is the electron charge, $\mu_n$ is the mobility, and $N_D$ is the doping concentration. This equation as is, is not very helpful since it does not allow us to directly estimate the specific resistance as a function of blocking voltage. To make it a function of blocking voltage, the impact ionization integral must be solved assuming the maximum electric field is applied. The result of this analytical solution gives the blocking voltage as a function of doping which can be used to also give the depletion width as a function of doping:

$$BV_{pp} = 5.34 \times 10^{13}\ N_D^{-\frac{3}{4}}$$

$$W_{pp} = 2.67 \times 10^{10}\ N_D^{-\frac{7}{8}}$$

These two equations in combination with the specific on resistance equation given previously can be used to calculate the specific on resistance as a function of blocking voltage. The mobility can be assumed constant for low doping concentration as in the case of Si MOSFETs (used $\mu = 1350\frac{cm^2}{Vs}$) giving the following equation:

$$R_{on,sp-ideal} = 5.93 \times 10^{-9} BV_{pp}^{2.5}$$

This resistance equation (8), was used in the main text as a means of estimating the losses of the inverter for a given area. With this information, the size of the inverter could be calculated for a given cooling power density, blocking voltage, and the remaining parameters of the inverter detailed in Chapter 1.

# Appendix B: Microcontroller Source Code

This source code was adapted from the application notes [17], [18], and [19] supplied by Microchip. The source code can be provided by request.

# Bibliography


[1] O. Zucker, “Electric motor/generator with multiple individually controlled turn-less structures,” 9,755,468, 2017.

[2] O. S. F. Zucker, P. K. L. Yu, and Y. M. Sheu, “GaN switches in pulsed power: A comparative study,” *IEEE Trans. Plasma Sci.*, 2014.

[3] O. S. F. Zucker, “Low voltage low current massively parallel high performance EM gun topology MEMS based manufacturing,” in *Digest of Technical Papers-IEEE International Pulsed Power Conference*, 2011.

[4] O. Zucker, “New Topologies in Electro-mechanical Systems - A New Paradigm,” presented in *2015 IEEE Pulsed Power Conference*, 2015.

[5] A. T. De Almeida, F. J. T. E. Ferreira, J. A. C. Fong, and C. U. Brunner, “Electric motor standards, ecodesign and global market transformation,” *Conf. Rec. - Ind. Commer. Power Syst. Tech. Conf.*, pp. 1–9, 2008.

[6] Siemens, “Electric propulsion components with high power densities for aviation,” 2015.

[7] “User’s Manual for Advanced Axial Flux Synchronous Motors and Generators EMRAX 268 / 268 VHML Technical Data Table (dynamometer test data).”

[8] “KJ Magnetics - Specifications.” [Online]. Available: https://www.kjmagnetics.com/specs.asp. [Accessed: 31-Aug-2018].

[9] C. J. M. Lasance, “Advances in High-Performance Cooling for Electronics,” *Electron. Cool.*, pp. 1–10, 2005.

[10] Y. Yao, D. C. Lu, and D. Verstraete, “Power Loss Modelling of MOSFET Inverter for Low-Power Permanent Magnet Synchronous Motor Drive,” *2013 1St Int. Futur. Energy Electron. Conf. (Ifeec 2013)*, pp. 849–854, 2013.

[11] J. R. Mevey, “Sensorless Field Oriented Control of Brushless Permanent Magnet Synchronous Motors,” Kansas State University, 2009.

[12] B. J. Baliga, *Fundamentals of Power Semiconductor Devices*. Springer, 2008.

[13] I. Rectifier, “StrongIRFET$^{TM}$ IRL6283MTRPbF Base part number Package Type Standard Pack Orderable Part Number Form Quantity IRL6283MTRPbF DirectFET Medium Can Tape and Reel 4800 IRL6283MTRPbF,” 2014.

[14] D. Meeker, “Finite Element Method Magnetics.” 2018.

[15] W. H. Yeadon *et al.*, “HANDBOOK OF SMALL ELECTRIC MOTORS McGraw-Hill,” 2001.

[16] A. Lidow, J. Strydom, M. de Rooij, and D. Reusch, *GaN Transistors for Efficient Power Conversion: Second Edition*, vol. 9781118844. Chichester, United Kingdom: John Wiley & Sons Ltd, 2014.

[17] Microchip, “dsPIC30F Family Reference Manual High-Performance Digital Signal

Controllers," no. Microchips Technology Inc, 2006.

[18] S. D'Souza and Microchip, "Sensored BLDC Motor Control Using dsPIC30F2010," pp. 1–20, 2004.

[19] J. Zambada, "Measuring Speed and Position with the QEI Module," pp. 1–12, 2005.